energies

MDPI

Article

Adaptive Variable Universe Fuzzy Droop Control Based on a Novel Multi-Strategy Harris Hawk Optimization Algorithm for a Direct Current Microgrid with Hybrid Energy Storage

Chen Wang [1], Shangbin Jiao [1,*], Youmin Zhang [2], Xiaohui Wang [3] and Yujun Li [1]

[1] Shaanxi Key Laboratory of Complex System Control and Intelligent Information Processing, Xi'an University of Technology, Xi'an 710048, China; 1180311029@stu.xaut.edu.cn (C.W.); leo@xaut.edu.cn (Y.L.)
[2] Department of Mechanical, Industrial and Aerospace Engineering, Concordia University, Montreal, QC H3G 1M8, Canada; ymzhang@encs.concordia.ca
[3] Xi'an Thermal Power Research Institute Co., Ltd., Xi'an 710054, China; wangxiaohui@tpri.com.cn
* Correspondence: jiaoshangbin@xaut.edu.cn

Abstract: In the off-grid photovoltaic DC microgrid, traditional droop control encounters challenges in effectively adjusting the droop coefficient in response to varying power fluctuation frequencies, which can be influenced by factors such as line impedance. This paper introduces a novel Multi-strategy Harris Hawk Optimization Algorithm (MHHO) that integrates variable universe fuzzy control theory with droop control to develop an adaptive variable universe fuzzy droop control strategy. The algorithm employs Fuch mapping to evenly distribute the initial population across the solution space and incorporates logarithmic spiral and improved adaptive weight strategies during both the exploration and exploitation phases, enhancing its ability to escape local optima. A comparative analysis against five classical meta-heuristic algorithms on the CEC2017 benchmarks demonstrates the superior performance of the proposed algorithm. Ultimately, the adaptive variable universe fuzzy droop control based on MHHO dynamically optimizes the droop coefficient to mitigate the negative impact of internal system factors and achieve a balanced power distribution between the battery and super-capacitor in the DC microgrid. Through MATLAB/Simulink simulations, it is demonstrated that the proposed adaptive variable universe fuzzy droop control strategy based on MHHO can limit the fluctuation range of bus voltage within ±0.75%, enhance the robustness and stability of the system, and optimize the charge and discharge performance of the energy storage unit.

Keywords: photovoltaic DC microgrid; adaptive variable universe fuzzy control; droop control; Harris Hawk Optimization algorithm

Citation: Wang, C.; Jiao, S.; Zhang, Y.; Wang, X.; Li, Y. Adaptive Variable Universe Fuzzy Droop Control Based on a Novel Multi-Strategy Harris Hawk Optimization Algorithm for a Direct Current Microgrid with Hybrid Energy Storage. *Energies* **2024**, *17*, 5296. https://doi.org/10.3390/en17215296

Academic Editor: Tek Tjing Lie

Received: 25 September 2024
Revised: 11 October 2024
Accepted: 21 October 2024
Published: 24 October 2024

1. Introduction

The increasing use of DC electrical equipment, along with advancements in Distributed Generation (DG) and power electronics technology, has sparked interest in DC microgrids due to their simple control, high reliability, and minimal energy loss [1–4]. To address the intermittent and random nature of photovoltaic (PV) power generation, energy storage systems (ESSs) are necessary in the DC microgrid to reduce the uncertainty of distributed renewable energy generation. This stabilizes the output and improves the operational stability of off-grid operation in the DC microgrid [5].

Hybrid energy storage systems (HESSs) are a prominent focus in energy storage technology research. Energy storage equipment is typically divided into two categories: energy storage and power storage [6]. Energy storage equipment, such as lead-acid batteries, provides long storage times and enables large-scale energy storage [7]. However, it is hindered by slow response speeds and short cycle lives, making it more suitable for load peak load shifting and voltage support than frequent charge and discharge cycles. On the other hand, power-type energy storage units, like super-capacitors (SCs), offer high power densities

and extended cycle lives, but are more adept at stabilizing intermittent energy fluctuations than long-term energy storage [8]. Currently, PV DC microgrid energy storage systems commonly incorporate a hybrid device that combines batteries and super-capacitors. This approach capitalizes on the high energy density of batteries and the high power density of SCs to effectively manage the power balance within the system, ensuring its safe and stable operation. Research in this field mainly focuses on developing optimal power allocation strategies for these hybrid energy storage units [9].

Zhou et al. [10] utilized a low-pass filter to split the frequency of load voltage and current signals, to evenly distribute missing power among different energy storage units. Wang et al. [11] replaced the low-pass filter with a high-pass filter and used the wavelet transform principle to divide the system's residual power. Xiao et al. [12] proposed an adaptive variational mode decomposition method to reduce fluctuations in PV output, thereby fully exploiting the advantages of the fast response speed of SCs and high energy density of batteries. However, this approach can lead to increased system costs and complexity and reduced system reliability. To overcome these challenges, decentralized droop control is implemented in DC microgrids, using impedance equivalent circuits to integrate droop coefficients and linearize bus voltage reference values for dynamic power distribution.

Anand et al. [13] constructed a steady-state mathematical model for a direct current (DC) microgrid, analyzing the impact of droop control on power distribution and the role of line impedance. However, this control strategy primarily optimizes the accuracy of steady-state power distribution and does not address the issue of power allocation among different types of energy storage devices. Xiao et al. [14] proposed a novel hierarchical control method for HESSs, utilizing centralized and distributed control. The bus voltage acts as a global indicator of the system power balance, with HESS control implemented through the droop relationship. Ding et al. [15] used a low-pass filtering algorithm to calculate the missing power target value and applied fuzzy adaptive theory to allocate this target power value between the battery and super-capacitor. Malik et al. [16] introduced an adaptive virtual capacitor droop for SCs in HESSs, utilizing a Switching Control Capacitor (SCC) to adjust the capacitance droop coefficient, affecting the absorption and release power of the storage component. Li et al. [17] proposed a droop-control-based method for power sharing in a HESSs that combines a Battery Energy Storage System (BES) and Superconducting Magnetic Energy Storage System (SMES). The droop control technique was used to prioritize charging/discharging in order to protect the battery from high power demands and rapid cycling.

Intelligent control techniques in the microgrid control strategy often involve complex optimization problems with non-differentiable objective functions, nonlinear search spaces, nonconvexity, and NP-hard problems [18]. Traditional optimization methods may not be effective in such cases, leading researchers to turn to stochastic methods like meta-heuristics, especially for real-world NP-hard optimization problems. Meta-heuristic algorithms can be broadly classified into 11 categories as follows: (1) evolutionary algorithms (Genetic Algorithm (GA) [19], differential evolution (DE) [20], etc.); (2) swarm-based algorithms (Particle Swarm Optimization (PSO) [21], Pied Kingfisher Optimizer (PKO) [22], Mountain Gazelle Optimizer [23], etc.); (3) ancient-based algorithms (Giza Pyramids Construction (GPC) [24], etc.); (4) physics-based algorithms (Simulated Annealing (SA) [25], Kepler Optimization Algorithm (KOA) [26], Light Spectrum Optimizer (LSO) [27], Equilibrium Optimizer (EO) [28], Golden Sine Algorithm (GSA) [29], etc.); (5) chemistry-based algorithms (Chemical Reaction Optimization (CRO) [30], Crystal Structure Algorithm (CryStAl) [31], etc.); (6) human-based algorithms (Sewing Training-Based Optimization (STBO) [32], Society Civilization Algorithm (SCA) [33], etc.); (7) plant-based algorithms (Invasive Weed Optimization (IWO) [34], Artificial Root Foraging Algorithm (ARFA) [35], etc.); (8) music-based/art-based algorithms (Harmony Search Algorithm (HSA) [36], Musical Composition Algorithm (MMC) [37]); (9) sport-based algorithms (Volleyball Premier League (VPL) [38], Running City game optimizer (RCGO) [39]); (10) mathematical-based algorithms (Arithmetic Optimization Al-

gorithm (AOA) [40], Sine-Cosine Algorithm (SCA) [41], etc.); and (11) single-solution-based algorithms (Large Neighborhood Search (LNBS) [42], Tabu Search (TS) [43], etc.). Harris Hawk Optimization is a novel algorithm introduced by Heidari et al. in 2019 [44]. The algorithm is characterized by its simple parameter setting, high solution accuracy, and robust global exploration capabilities during basic performance tests. However, shortcomings such as limited population diversity in initialization and a singular method of updating population positions result in slow convergence and susceptibility to local optimization during the iterative process.

Based on the above analysis, previous research has demonstrated that while the fuzzy control droop method can improve the dynamic response speed of HESSs by adjusting the initial droop coefficient [45]. But it does not address the optimal distribution of charging and discharging power for individual batteries and super-capacitors as their State of Charge (SOC) changes. Additionally, integrating SOC compensation for batteries and super-capacitors in a HESSs introduces stronger nonlinear characteristics, making the fuzzy control rule base insufficient and significantly reducing the accuracy of traditional fuzzy controllers.

This paper introduces an adaptive variable universe fuzzy control strategy that utilizes a Multi-strategy Harris Hawk Optimization Algorithm (MHHO) to dynamically adjust the droop coefficient of batteries and super-capacitors in real-time. The variable universe fuzzy control enhances droop control and optimizes the droop coefficient on-the-fly. A novel MHHO is proposed in this study, incorporating Fuch mapping, golden sine strategy, and a newly designed elitism lens imaging opposition-based learning strategy to enhance performance. The effectiveness of the algorithm is evaluated by comparing it with five classical meta-heuristic algorithms, HHO, KOA, LSO, EO, and PKO, on the CEC2017 benchmarks. The proposed algorithm focuses on adaptive variable universe fuzzy control to dynamically adjust the fuzzy control universe in real-time. This allows for the battery to compensate for low-frequency power shortages and the super-capacitor to address high-frequency power shortages. By effectively distributing power fluctuations with different frequency characteristics among HESS units, the proposed method mitigates the negative impact of internal factors like load changes and line impedance on power distribution. This decentralized approach operates independently of communication links, reducing the risk of delays and single points of failure in centralized control. As a result, the method offers easy implementation for plug-and-play control in practical systems, enabling flexibility in system structure and operational modes. Additionally, MATLAB/Simulink simulations show that the adaptive variable universe fuzzy-droop control strategy based on the MHHO effectively regulates power in DC microgrids, ensures stable DC bus voltage operation, and enhances system robustness.

Compared with previous work, this paper offers the following contributions:

1. To achieve an optimal distribution of power fluctuations with varying frequency characteristics among HESS units, this study enhances droop control through variable universe fuzzy control and real-time optimization of the droop coefficient. The battery appropriately compensates for low-frequency power shortages, while the super-capacitor effectively addresses high-frequency power shortages. This approach eliminates the adverse effects of internal factors like load mutations and line impedance on power distribution, thereby ensuring the safe and stable operation of the system.
2. A new MHHO is proposed by introducing Fuch mapping in the population initialization. In the exploration and exploitation phase, the golden sine strategy is introduced and a new elitism lens imaging opposition-based learning strategy is designed to improve the convergence ability of the HHO algorithm. The CEC2017 test function is compared with five new meta-heuristic algorithms to verify the excellent numerical performance of the proposed algorithm.
3. The droop control of hybrid energy storage based on adaptive variable universe fuzzy logic algorithm has not been reported in previous work. By integrating the effective search capability of the MHHO algorithm with the dynamic adjustment ability of

variable universe fuzzy control to the droop curve, an adaptive variable universe fuzzy droop control based on MHHO is developed. This control system adjusts the droop coefficient adaptively to mitigate the impact of line impedance on power distribution and enhance the precision of power sharing.

4. Simulation and experimental results verify the correctness and effectiveness of the proposed method.

This paper is structured as follows: Section 2 outlines the configuration of a PV DC microgrid system. Section 3 introduces the concept of fuzzy droop control and its implementation. Additionally, a new MHHO is designed and applied to variable universe fuzzy control in Section 3. Section 4 presents the simulation results to evaluate the performance of the proposed method. Finally, the conclusion is drawn in the last section.

2. Photovoltaic DC Microgrid System Structure

2.1. System Structure

The structure of the PV DC microgrid system constructed in Figure 1, which is mainly composed of photovoltaic cells, battery, super-capacitor, loads, and various DC converters. The photovoltaic cell is connected to the DC bus via the Boost converter and operates in maximum power point (MPPT) mode [46]. The battery and super-capacitor are connected to the DC bus through a Bidirectional DC/DC Converter (BDC) that enables bidirectional energy flow and compensates for system power imbalances to ensure safe and stable operation. The system's load comprises ordinary resistive and motor loads connected in parallel to the DC bus through a Buck converter.

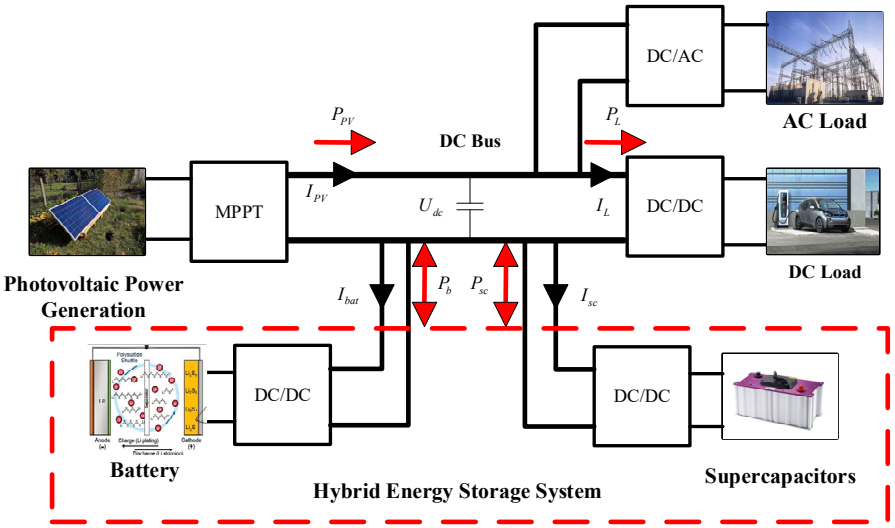

Figure 1. Structural diagram of photovoltaic DC microgrid system.

2.2. Topological Structure of Main Circuit

The main circuit topology of the PV DC microgrid in the off-grid state is illustrated in Figure 2. Main circuit topology of DC microgrid. U_{bat} and U_{sc} denote the terminal voltage (V) of the battery and the SC respectively. L_{bat} represents the energy storage inductance (H) of the battery; L_{sc} is the energy storage inductance (H) of the SC; R_{bat} and R_{sc} stand for the parasitic resistance (Ω) of the battery and super-capacitor energy storage inductors, respectively. By applying Kirchhoff's current theorem, the dynamic equation of the DC microgrid can be derived as follows:

$$C_{\mathrm{dc}}\frac{\mathrm{d}u_{\mathrm{dc}}}{\mathrm{d}t} = (i_{\mathrm{b\_dc}} + i_{\mathrm{se\_dc}} + i_{\mathrm{pv\_dc}}) - i_{\mathrm{load}} - i_{\mathrm{d}} \quad (1)$$

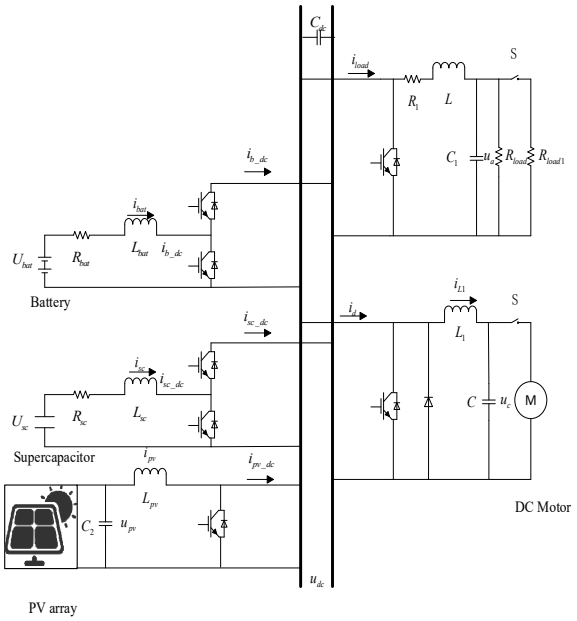

Figure 2. Main circuit topology of DC microgrid.

In Equation (1), C_{dc} represents the DC bus capacitor, U_{dc} represents the DC bus voltage, i_{pv_dc} represents the output current of photovoltaic cells, i_{b_dc} represents the output current of the battery, i_{sc_dc} represents the output current of the SC, and i_{load} represents the load current. The relationship outlined in Equation (1) shows that the output current of the photovoltaic cell i_{pv_dc} and the load current i_{load} impact the DC bus voltage. By managing the charging and discharging currents of the battery and super-capacitor in the HESSs, fluctuations in bus voltage can be minimized, enhancing the stability of the microgrid.

2.3. Photovoltaic Unit Module

PV unit is generally composed of photocurrent source, equivalent diode, series resistance R_s, parallel resistance R_{sh} and so on [47]. The equivalent model of photovoltaic unit is shown in Figure 3.

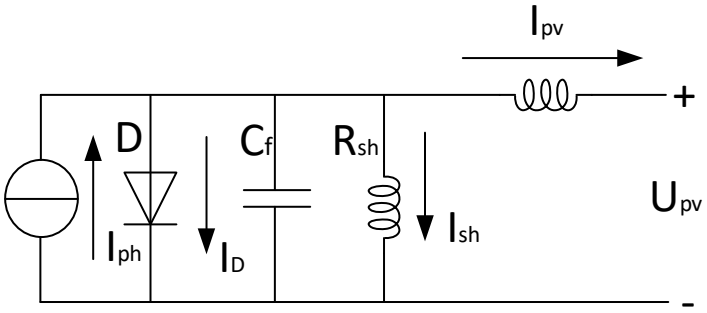

Figure 3. The equivalent model of a photovoltaic unit.

Let I_{ph} represent the photo-generated current source, I_D denote the current at the PN junction, and I_{pv} signify the output current of the photovoltaic unit. When the light intensity is constant, I_{pv} remains stable and does not vary. The model of the solar cell in an ideal state is described by a transcendental exponential equation, resulting in a nonlinear output characteristic that is influenced by numerous factors.

In practical engineering, the performance of photovoltaic power generation systems is significantly influenced by external factors. To manage this, MPPT control and constant voltage control are commonly employed. Currently, MPPT technologies primarily consist of several methods, including the constant voltage control method, conductance increment method, perturbation observation method, and fuzzy control method [47]. Among these,

the perturbation observation method (P&O) is particularly popular due to its straightforward principle and effective optimization results.

2.4. Hybrid Energy Storage Unit Model

In the PV DC microgrid with HESS, batteries typically serve as the primary energy storage devices, while SC function as auxiliary energy storage units [48]. When the power generation from the PV system becomes unstable, the battery engages in charging and discharging to absorb or compensate for excess energy within the microgrid. However, excessive charging and discharging can adversely affect the battery's lifespan. Although super-capacitors have significantly lower energy storage capacity compared to batteries, their charging and discharging processes are based on physical mechanisms, allowing for a greater number of cycles and an extended lifespan. Given these considerations, it is advantageous to employ a combination of batteries and super-capacitors for energy storage. In this arrangement, the super-capacitor accommodates high-frequency power demands, while the battery primarily handles low-frequency power requirements, thereby collectively ensuring the stability of the microgrid.

(1) The model of a battery

In this paper, the Thevenin equivalent circuit model is employed to analyze the battery, and its representation is illustrated in Figure 4. It consists of a DC voltage source E, a polarization resistor R_e, a polarization capacitor C_e, and internal resistance R_b.

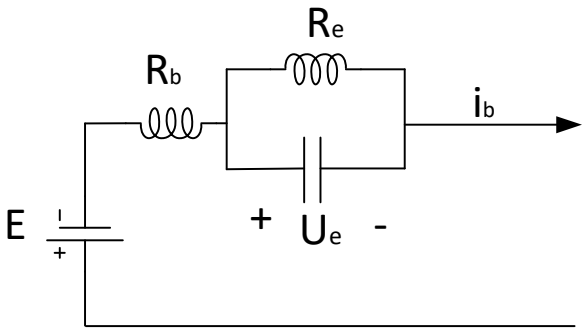

Figure 4. Thevenin equivalent circuit model.

During the operation of a battery, its internal resistance and terminal voltage are influenced by both the battery's inherent capacity and variations in external temperature. Typically, the *SOC* is utilized to represent the remaining energy in the battery, which can be expressed as follows:

$$SOC = \frac{Q}{C} \tag{2}$$

In the above formula, Q denotes the remaining capacity of the battery, while C represents the rated storage capacity. Batteries are nonlinear energy storage devices, making accurate prediction of their real-time SOC challenging. Generally, the ampere-hour integration method is employed for estimation. If the initial SOC value of the battery is known, the real-time charging and discharging currents can be estimated accordingly.

$$SOC(t) = SOC(t_0) - \frac{1}{C}\int_{t_0}^{t} i(t)dt \tag{3}$$

In the above formula, $SOC(t_0)$ is the initial state of the battery.

(2) The model of a super-capacitor

The equivalent series resistance depicted in Figure 5a diminishes the charging efficiency of the SC, with its resistance value R_{sc} typically being relatively low. Conversely, the leakage current I_{sc} associated with the equivalent parallel resistance R_c adversely affects the energy storage performance of the super-capacitor, where the resistance value is generally

higher. In practical applications, SCs undergo frequent charging and discharging cycles, which have a negligible impact on their operational characteristics. Consequently, the simplified equivalent model of the SC comprises an ideal capacitor C_{sc} in series with an equivalent series resistance R_{sc}.

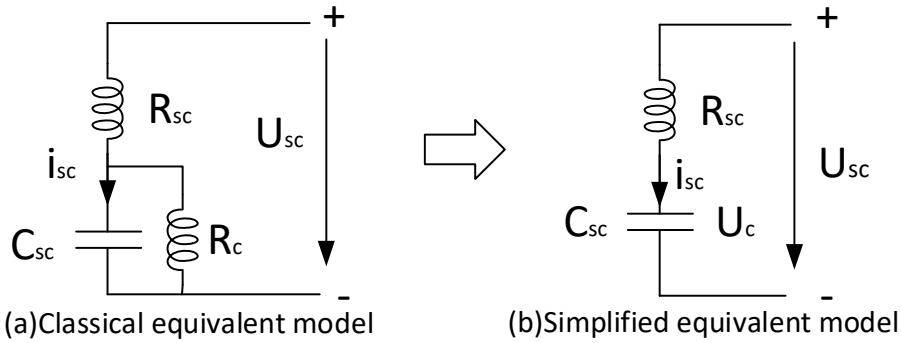

Figure 5. The equivalent mathematical model of the super-capacitor.

The RC equivalent circuit model is

$$u_{sc} = I_{sc}.R_s + \frac{1}{C}\int i_{sc}dt \tag{4}$$

The SOC of the SC can be expressed as

$$SOC = \frac{Q_t}{Q_N} = \frac{C(u_{sc} - u_{\min})}{C(u_{\max} - u_{\min})} = \frac{u_0 + \frac{1}{C}\int_0^t i_{sc}dt - u_{\min}}{u_{\max} - u_{\min}} \tag{5}$$

In the formula above, Q_N is the total charge of the SC, Q_t is the charge of the SC at time t, $u_{\max}$ and $u_{\min}$ represent the maximum and minimum operating voltages of the SC, respectively, and u_0 is the initial voltage value.

2.5. The Model and Control Strategy of the DC Motor

The model of the DC motor

In normal operating conditions, the power change of a typical resistive load remains relatively stable, and significant power fluctuations do not occur when the switch is either closed or disconnected [49]. However, the DC bus voltage is influenced when an impact load is connected or disconnected. To investigate the effects of the impact load on system stability, this paper focuses on the DC motor as the load side component of the PV DC microgrid. The ideal equivalent circuit is illustrated in Figure 6.

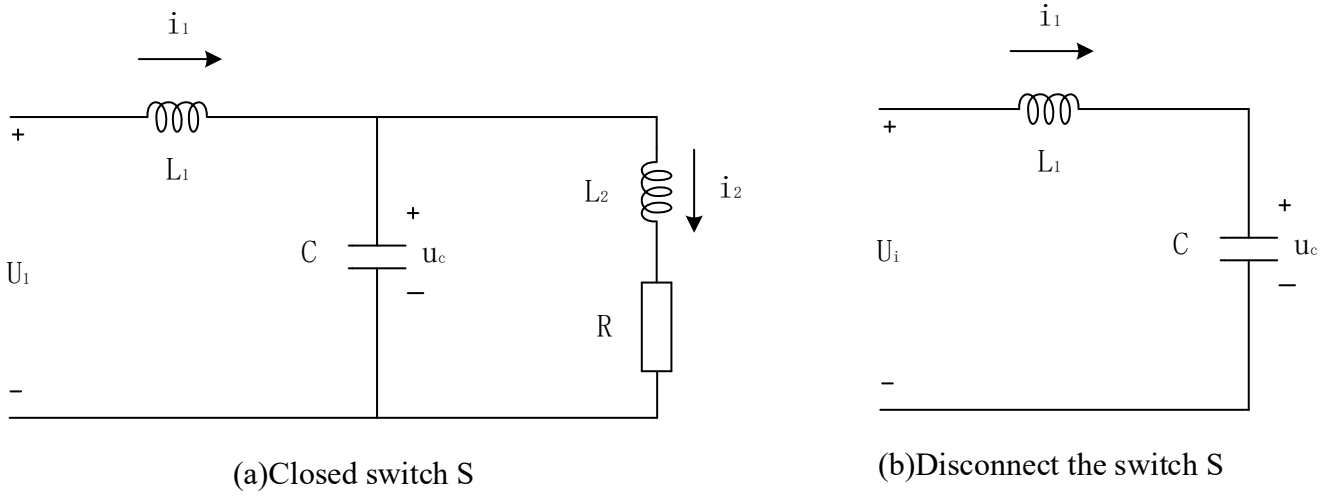

Figure 6. The ideal equivalent circuit of a DC motor.

In the Figure 6, L_1 and L_2 represent the energy storage inductance and the equivalent inductance of the DC motor, respectively. C denotes the filter capacitor at the load end; S represents the load switch; R indicates the equivalent resistance of the load; i_1 and i_2 are the load current; U_i is the terminal voltage of the DC motor; and u_c is the motor input voltage. When the switch S is closed, the DC motor is connected to the main circuit, as illustrated in the equivalent circuit diagram shown in Figure 6a. This configuration is analyzed using Kirchhoff's voltage and current laws:

$$\begin{cases} U_{\mathrm{i}} = L_1 \frac{di_1}{dt} + u_c \\ u_c = L_2 \frac{di_2}{dt} + i_2 R \\ i_1 = C \frac{du_c}{dt} + i_2 \end{cases} \tag{6}$$

The switch S is disconnected, and the DC motor is disconnected from the main circuit. The equivalent circuit diagram is shown in Figure 6b. It is listed by Kirchhoff's voltage and current law:

$$D = \frac{t_{\mathrm{on}}}{t_{\mathrm{on}} + t_{\mathrm{off}}} \tag{7}$$

The impact load is connected in parallel to the DC bus via the Buck converter, with the DC bus voltage set at 650 V. The Buck converter reduces this voltage level to supply power to the DC motor. Here, U_M^* represents the calibration value of the DC motor's terminal voltage at the load end, while U_M denotes the output voltage value of the DC motor at the same point. The difference between U_M^* and U_M serves as the input signal for the load terminal voltage controller. The control signal for the Buck step-down converter is derived from the voltage and current controller, ensuring the stable operation of the DC motor system.

2.6. Modeling Power Converters

(1) Characterization of photovoltaic-side power converter operation

The PV unit transmits energy to the DC bus through the Boost converter to maintain the stable operation of the system. The topology of the Boost converter is shown in Figure 7.

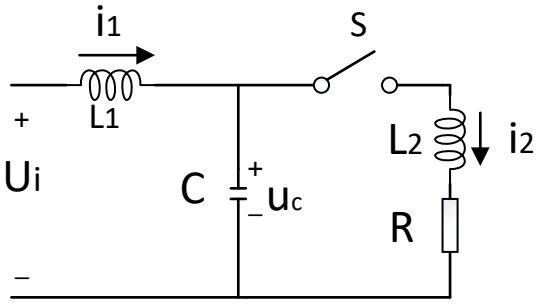

Figure 7. The topology of the Boost converter.

There is the following relationship between the input voltage U_{pv} and the output voltage U_{dc} in the Boost circuit:

$$D = \frac{t_{\mathrm{on}}}{t_{\mathrm{on}} + t_{\mathrm{off}}} \tag{8}$$

$$\begin{cases} U_{\mathrm{dc}} = \frac{1}{1-D} U_{\mathrm{pv}} \\ i_0 = (1-D) i_{\mathrm{pV}} \end{cases} \tag{9}$$

In Equations (8) and (9), t_{on} and t_{off} are the turn-on and turn-off time of the switch tube, i_{pv} is the current of the PV unit, and i_0 is the current of the output end of the Boost converter.

(2) The operating characteristics of the energy storage power converter

Bidirectional DC/DC converter is composed of switches and diodes, which is a strong nonlinear power electronic device. In this paper, an isolated bidirectional DC/DC converter with high efficiency and high power density is selected.

In Figure 8, U_0 is the terminal voltage of the energy storage unit, and U_{dc} is the DC bus voltage. The working mode of the power converter is determined by turning on or turning off the switch tube S1 and S2. When the energy storage unit works in the discharge state in order to compensate the power difference of the system, the bidirectional DC/DC converter is in the Boost mode, and i_L is the current flowing through the inductor on the energy storage side. When the switch tube S1 is disconnected and S2 is turned on, the energy storage unit releases energy to charge the inductor L.

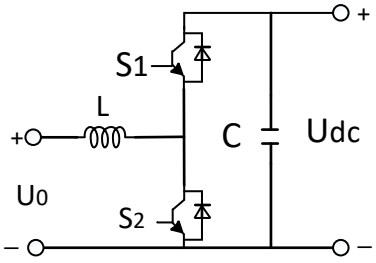

Figure 8. Bidirectional DC/DC converter.

The relationship between the energy storage terminal voltage and the bus voltage in Boost mode is

$$U_{\mathrm{dc}} = \frac{t_{\mathrm{on}} + t_{\mathrm{off}}}{t_{\mathrm{off}}} U_0 \tag{10}$$

The relationship between the energy storage terminal voltage and the bus voltage in Buck mode is

$$U_{\mathrm{dc}} = \frac{t_{\mathrm{on}}}{t_{\mathrm{on}} + t_{\mathrm{off}}} U_0 \tag{11}$$

U_0 is the terminal voltage of the energy storage unit, U_{dc} is the DC bus voltage, t_{on} and t_{off} are the turn-on and turn-off time of the switch tube, respectively.

(3) Grid-connected inverter model and control strategy

The grid inverter serves as the connection link between the DC microgrid and the distribution network. It is categorized into two types: a current-source three-phase inverter that regulates the output current, and a voltage-source three-phase inverter that manages the output voltage. In this paper, we focus on the voltage-source three-phase inverter, with the following default settings: (1) three-phase voltage balance of the microgrid; (2) the filter inductor is treated as a linear device, without accounting for saturation; and (3) switches S1 to S6 are considered ideal devices, with their losses disregarded. The topology of the three-phase inverter is illustrated in Figure 9.

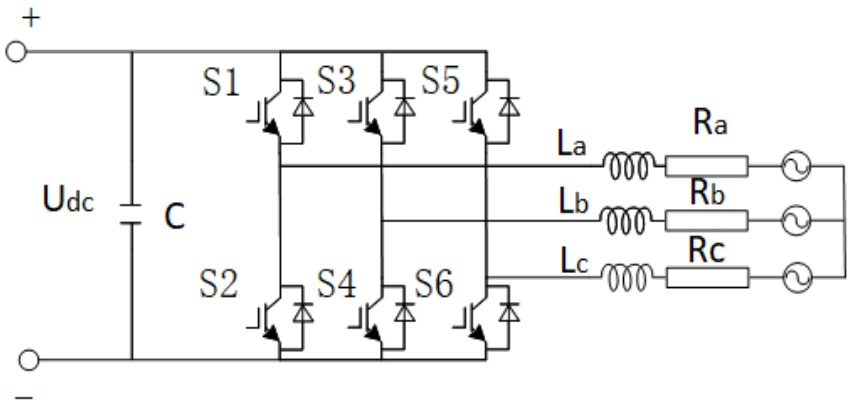

Figure 9. The topology of the three-phase inverter.

Figure 9 shows the DC bus voltage, U_{dc} is the DC side filter capacitor, U_a, U_b and U_c are the inverter terminal voltage, L is the filter inductor, R is the equivalent resistance, and e_a, e_b are e_c the three-phase power supply voltage, i_a, i_b and i_c are the inverter bridge arm side current. To simplify the controller design of the inverter, the three-phase stationary coordinate system is transformed from Clack (abc $\rightarrow$ $\alpha\beta$) to Park ($\alpha\beta \rightarrow$ dq0), resulting in the DC component represented in the dq0 coordinate system, which maintains the same fundamental frequency as the microgrid. This transformation alleviates the complexity associated with the inverter's controller design. The grid-connected DC/AC inverter employs a voltage outer loop and a current inner loop with feedforward decoupling control, while the current regulator utilizes PI control. PI controller can effectively balance the steady-state and dynamic performance of a control system. By incorporating a current inner loop within the voltage loop, the system's dynamic response speed can be significantly enhanced, thereby reducing the impact of load disturbances in a timely manner. The control strategy block diagram is illustrated in Figure 10.

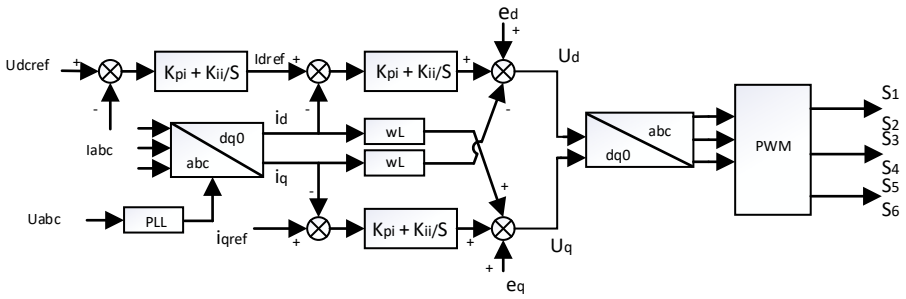

Figure 10. The controller design of the inverter.

3. Fuzzy Droop Control Strategy

3.1. Classical Droop Control

Currently, the energy storage unit in a PV DC microgrid typically employs a double closed-loop control system for voltage and current [50]. The DC bus voltage serves as the outer loop control, while the energy storage inductor current functions as the inner loop control. Additionally, droop control is commonly integrated into the double closed-loop control system to provide a voltage reference value. Droop control methods include I-U droop control and P-U droop control. For instance, the control block diagram for I-U droop control is illustrated in Figure 11.

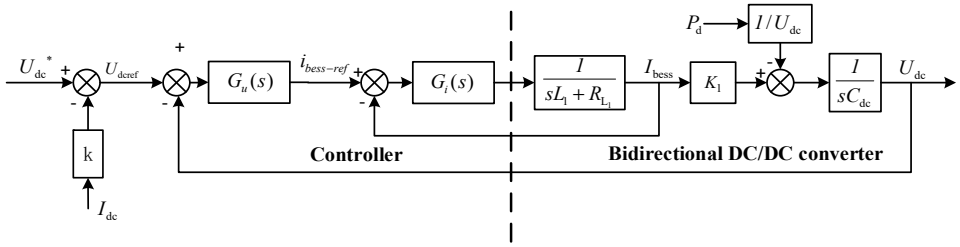

Figure 11. The control block diagram for I-U droop control.

Figure 3 illustrates the components involved in the control block of HESSs, including voltage outer loop PI controller $G_u(s)$, current inner loop PI controller $G_i(s)$, inductance value of the freewheeling inductor L_1, impedance value of the energy storage device R_{L1}, output current of the energy storage device i_{bess}, bus capacitance value C_{dc}, disturbance power P_d, and proportional gain K_1. Assuming that the internal resistance and internal voltage of each energy storage unit are zero, ignoring the line impedance, the traditional droop control relationship is shown in Equation (12):

$$U_{\text{deref}} = U_{\text{dc}}^* - kI_{\text{dc}} \tag{12}$$

In the above formula, U_{deref} represents the voltage reference value for droop control; U_{deref} is the stable value of bus voltage; I_{dc} is the output current value of the energy storage system; and k is the droop coefficient.

3.2. Limitations of Traditional Droop Control

To investigate the power distribution among multiple energy storage units using the traditional droop control strategy, the simplified equivalent circuit of the microgrid is depicted in Figure 12.

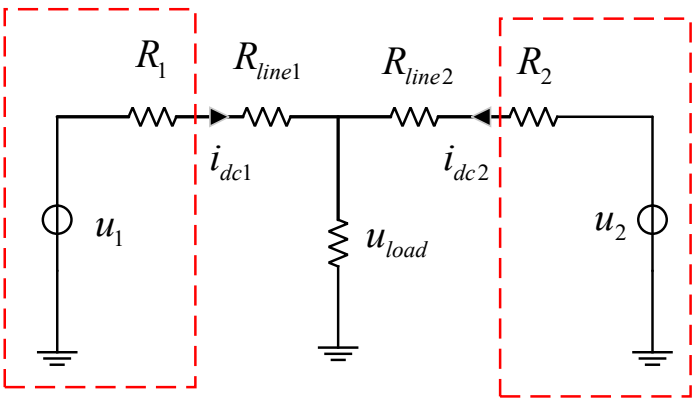

Figure 12. Simplified equivalent circuit of DC microgrid.

In Figure 12, R_1 and R_2 denote the equivalent output impedances of converter 1 and converter 2, respectively. R_{line1} and R_{line2} represent the cable impedance between converter 1, converter 2, and the bus. i_{dc1} and i_{dc2} indicate the output current of converter 1 and converter 2, respectively. u_{dc1} and u_{dc2} stand for the output voltage of converter 1 and converter 2, respectively. u_{load} is the load terminal voltage; the initial given voltages of converter 1 and converter 2 are denoted as u_1 and u_2, respectively. Assuming $u_1 = u_2$, the relationship between the output currents of the two converters is as follows:

$$\frac{i_{\text{del}}}{i_{\text{de2}}} = \frac{R_2 + R_{\text{line2}}}{R_1 + R_{\text{line1}}} \tag{13}$$

The relationship between the output current of energy storage converter 1 and converter 2, as per Equation (13), depends on their equivalent output impedance and cable impedance. Droop control in the energy storage converter acts like a virtual impedance in series, increasing the converter's equivalent output impedance. The traditional droop control method does not take into account the cable impedance between each energy storage converter and the DC bus, and the impedance of these cables can vary significantly. In order to the output current of the energy storage converter to be inversely proportional to the droop coefficient, the ratio of the cable impedance of each converter must be equal to the ratio of its droop coefficient. Under this condition, the cable impedance does not affect the accuracy of power distribution in the system. However, achieving this ideal scenario is challenging in practical implementation. When the line impedance of the converter in a system is large, neglecting the cable impedance can result in a reduction in the accuracy of power allocation for the energy storage unit. In such cases, the most effective approach is to increase the droop coefficient to enhance the power allocation accuracy among the energy storage units. However, raising the droop coefficient may lead to a decrease in the DC bus voltage regulation capability.

Figure 13 illustrates the constraints of traditional droop control. Assuming that the output power and virtual impedance of the energy storage unit converter are equal, but the cable impedance differs, the droop curves of the two energy storage converters will not be the same. When the droop coefficient is small, the shunt deviation between points i_1 and i_2 is Δi, resulting in a bus voltage deviation of Δu. On the other hand, when

the droop coefficient is large, the shunt deviation between points i_1' and i_2' is $\Delta i'$, with a corresponding bus voltage deviation of $\Delta u'$. Through the above analysis, it is evident that decreasing the droop coefficient can minimize bus voltage deviation, albeit at the expense of power allocation accuracy. Conversely, increasing the droop coefficient can enhance the power allocation accuracy of the energy storage unit, but may lead to a higher bus voltage deviation.

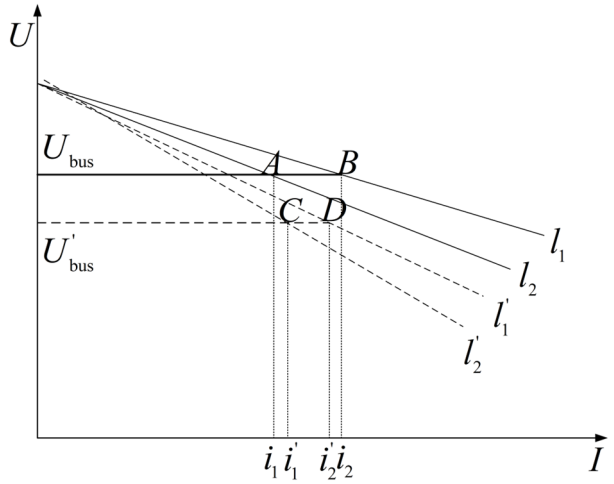

Figure 13. Droop control curve diagram.

The traditional droop control method faces challenges in effectively allocating load power due to its fixed droop coefficient. As a result, changes in the SOC of the batteries can lead to imbalanced SOC levels among them. To address this issue, integrating the SOC value of the battery into the droop coefficient is necessary. This adjustment ensures that batteries with lower SOC values receive smaller droop coefficients during charging, leading to increased charging power and faster charging speeds. Conversely, batteries with higher SOC values receive smaller droop coefficients during discharging, enabling higher discharge power and faster discharge rates. This approach aims to achieve a balanced SOC among batteries. It is evident that the traditional droop control method has limitations in balancing power distribution accuracy for energy storage units and minimizing bus voltage deviations.

3.3. Fuzzy Droop Control of Hybrid Energy Storage System

The traditional droop control method encounters difficulties in appropriately assigning droop coefficients based on power fluctuations with varying frequency characteristics. Moreover, unpredictable factors such as load mutations within the system can influence the allocation characteristics. Consequently, traditional droop control struggles to ensure precise power allocation among HESS units. This research merges the characteristics of a fuzzy control algorithm with droop control to develop droop coefficients for charging and discharging processes. The adjustment law for droop coefficients takes into account output power, SOC, and DC bus voltage to minimize bus voltage fluctuations around its rated value. The energy storage device effectively stabilizes bus voltage in response to external changes or variable loads, improving the system's anti-interference capabilities. Throughout charging and discharging, the energy storage device optimizes power distribution based on SOC values, ensuring that devices with low SOC receive high charging power and low discharge power, while devices with high SOC receive low charging power and high discharge power. Real-time dynamic adjustment of droop coefficients and optimization of the droop curve facilitate efficient power distribution in HESS units [48,51]. Due to the distinct working characteristics of batteries and SCs, separate fuzzy-droop controllers are recommended for each to achieve precise power distribution. To accomplish this, unbal-

anced power should be divided based on frequency, with low-frequency power assigned to batteries and high-frequency power allocated to SCs.

Firstly, Equation (12) is transformed to express the product of virtual impedance R_{xi} and output current I_{dc} as output power P_i, and the droop coefficient R_i is redefined. The droop control formula is then modified to Equation (14), U_{dc}^{*} representing the expected value of the bus voltage:

$$U_{\mathrm{deref}} = U_{\mathrm{dc}}^{*} - R_i P_i \tag{14}$$

The droop coefficient R_i (i = 1, 2) of the battery discharge, as outlined in Reference [51], is inversely proportional to SOC^n value of the battery. A droop coefficient adjustment law k is then designed based on the bus voltage:

$$R_{bat} = \frac{k_{bat}}{SOC_{bat}^{n}} \tag{15}$$

$$R_{sc} = \frac{k_{sc}}{SOC_{sc}^{n}} \tag{16}$$

The above equations involve the index of SOC, denoted as n (n > 0), which impacts the SOC equalization speed. The droop coefficients for the battery and super-capacitor branches are represented as k_{bat} and k_{sc}. The fuzzy-droop control principle is illustrated in Figure 14, where the droop coefficients for both branches are shown. The DC bus voltage u_{dc}, P_{bat} is system's missing power, and P_{sc} is power response of the super-capacitor branch are also included in the diagram.

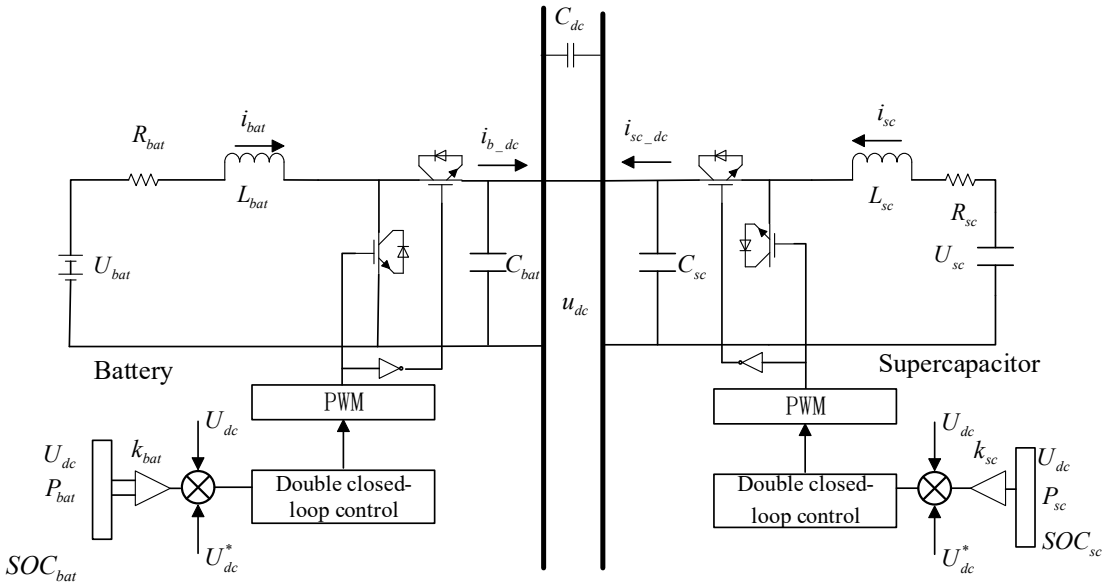

Figure 14. Adaptive variable universe fuzzy droop controller based on MHHO.

3.3.1. Fuzzy Droop Control in the Battery Branch

The fuzzy droop controller in the battery branch is designed to detect voltage fluctuations in the bus and adjust the output power of the battery accordingly [52]. By using fuzzy rules and reasoning, real-time adjustments are made to the droop coefficient, as illustrated in Equation (17):

$$k_{bat} = \int_0^t k(\tau)\mathrm{d}\tau \tag{17}$$

The droop coefficient of the battery is denoted as k_{bat}. The DC bus voltage reference value is set at 650 V, with the output voltage fluctuation range of the power supply system between 630 V and 670 V. The battery's output power is set between −10 kW and 70 kW. The membership functions for input u_{dc} and P_{bat} as well as the output k_{bat} are depicted in Figures 15–17, respectively. Fuzzy subsets for u_{dc} are defined as follows: S_3, S_2, S_1, CE, B_1, B_2,

B_3; Fuzzy subsets for P_{bat} are defined as follows: CE, NB, NM, NS, ZO, PS, PM, PB; Fuzzy subsets for k_{bat} are also categorized as NB, NM, NS, ZO, PS, PM, PB. By applying fuzzy control theory and considering the membership functions of input and output, fuzzy control rules are established, as detailed in Table 1. Utilizing the fuzzy control rules outlined in Table 1. Fuzzy control rules of k_{bat}. for the output k, the output surface observation diagram for the fuzzy droop control of the battery branch can be visualized in Figure 18.

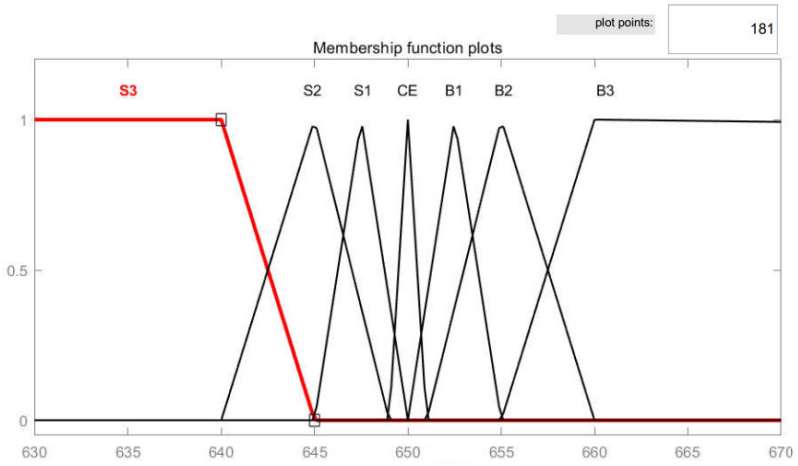

Figure 15. Membership functions of u_{dc}.

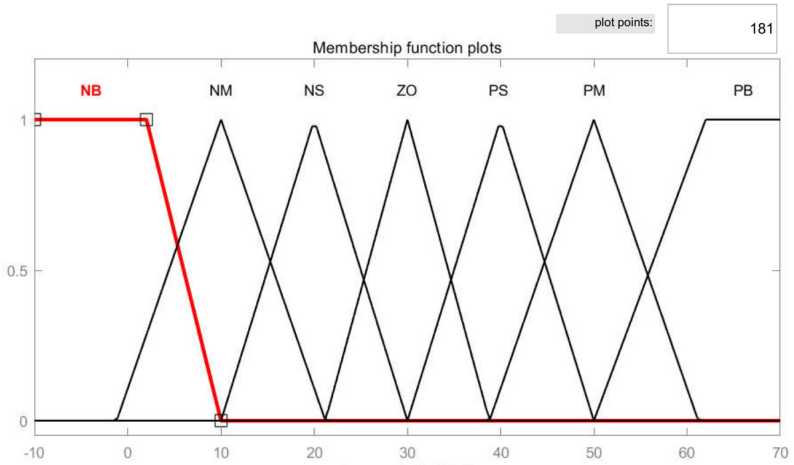

Figure 16. Membership functions of P_{bat}.

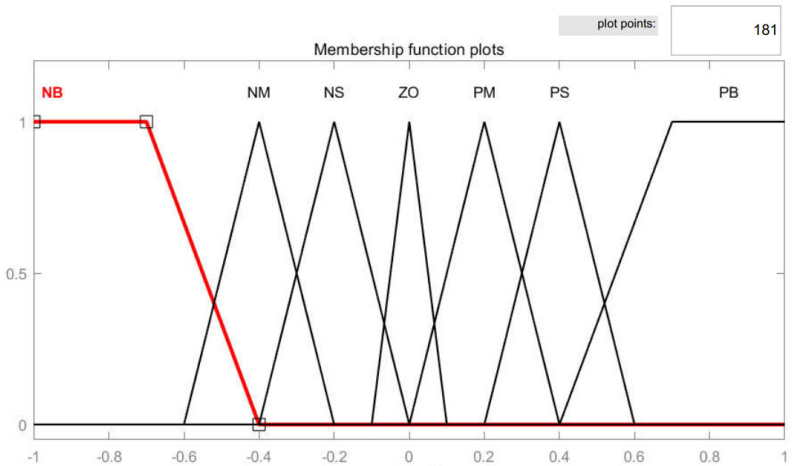

Figure 17. Membership functions of k_{bat}.

Table 1. Fuzzy control rules of k_{bat}.

$U_{dc}\backslash\Delta P$	NB	NM	NS	ZO	PS	PM	PB
S_3	PB	PB	PM	PS	NS	NS	NM
S_2	PB	PB	PM	PS	NS	NS	NM
S_1	PB	PM	PS	ZO	NS	NM	NB
CE	PB	PM	PS	ZO	NS	NM	NB
B_1	PB	PM	PS	ZO	NS	NM	NB
B_2	PB	PS	PS	ZO	NM	NB	NB
B_3	PB	PS	PS	ZO	NM	NB	NB

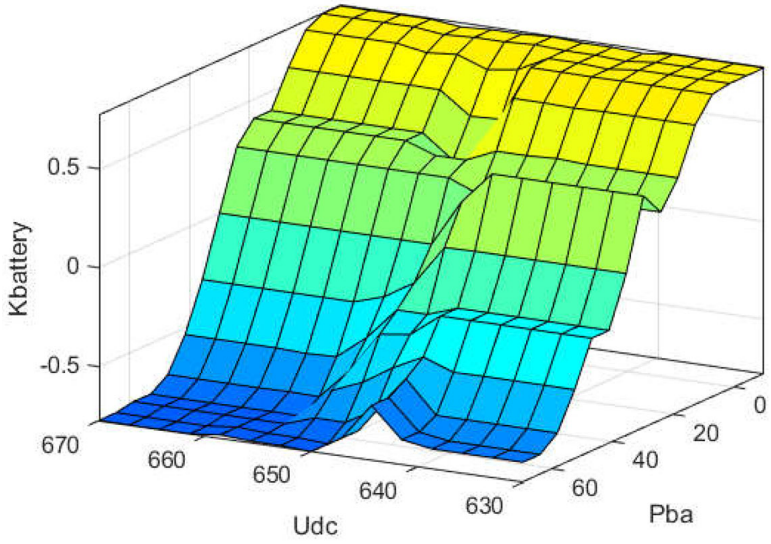

Figure 18. Surface observation graph of k_{bat}.

3.3.2. Fuzzy Droop Control of Super-Capacitor Branch

The fuzzy droop controller in the super-capacitor branch is responsible for detecting the voltage fluctuations of the bus and the output power of the super-capacitor. These parameters serve as inputs for the fuzzy controller, enabling the dynamic adjustment of the droop curve coefficient of the super-capacitor branch. The fuzzy control output follows the same formula as the battery branch, as shown in Equation (18):

$$k_{sc} = \int_0^t k(\tau)\mathrm{d}\tau \tag{18}$$

The droop coefficient of the battery is represented by k_{sc}. The value range of u_{dc} is the same as mentioned earlier, while the value range of P_{sc} is between -10 and 70 kW/s. The membership functions for the inputs u_{dc} and P_{sc}, as well as the output k′, are illustrated in Figures 19–21, respectively. Based on the control quantity's value range, the fuzzy subsets for u_{dc} are designated as P_1, P_2, P_3, P_4, P_5; for P_{sc}, as D1, D2, D3, D4, D5, D6, D7; and for k_{sc}, as k1, k2, k3, k4, k5, k6, k7. By applying fuzzy control theory and considering the membership functions of inputs and outputs, the fuzzy control rules for k_{sc} are derived and presented in Table 2.

As the power change rate of the SC decreases, the output power will gradually decrease, requiring a reduction in the droop coefficient. Conversely, when the power change rate of the SC increases, the output power will gradually increase, necessitating an increase in the droop coefficient. By following the fuzzy control rules outlined in Table 2 for the output k_{sc}, the output surface observation diagram for the fuzzy-droop control of the SC branch can be generated, as depicted in Figure 22.

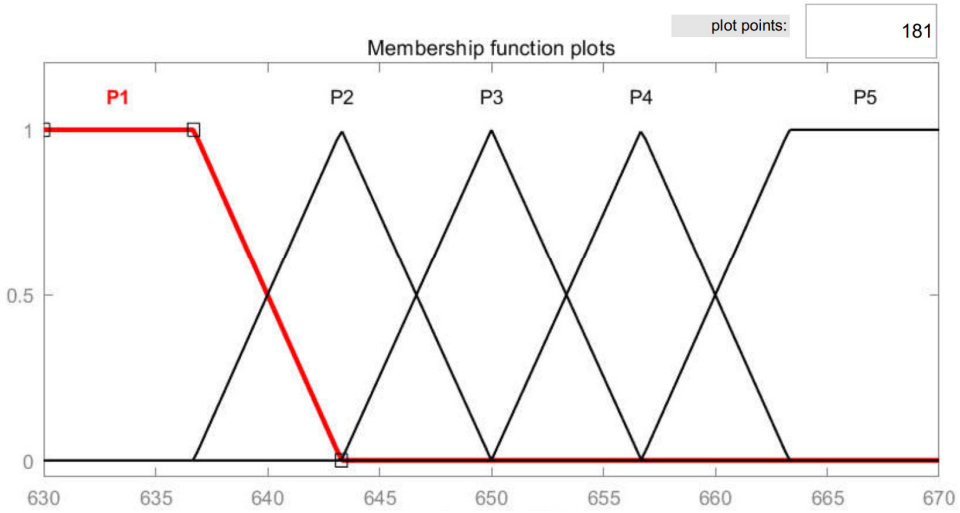

Figure 19. Membership functions of u_{dc}.

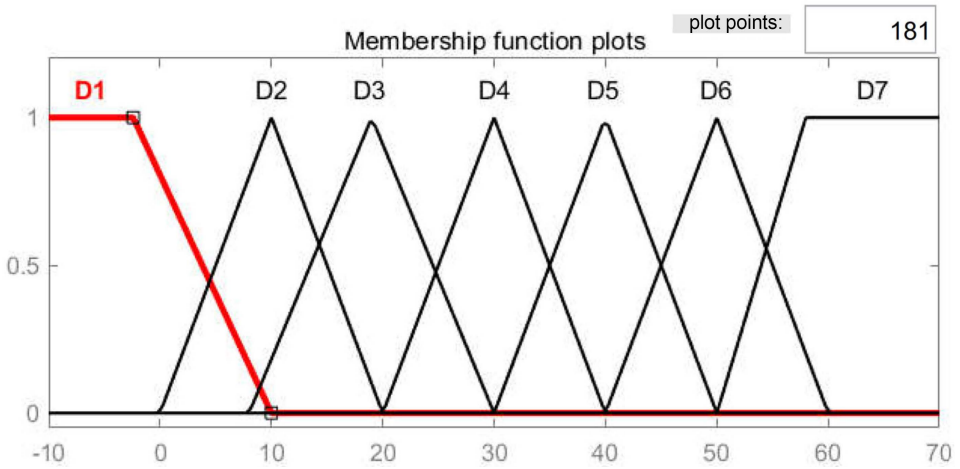

Figure 20. Membership functions of P_{sc}.

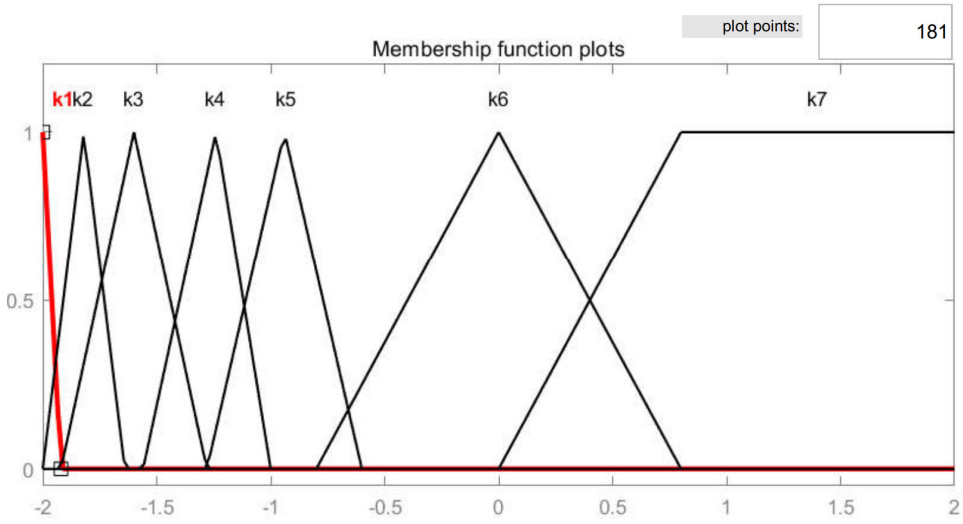

Figure 21. Membership functions of k_{sc}.

Table 2. Fuzzy control rules of k_{sc}.

	D_1	D_2	D_3	D_4	D_5	D_6	D_7
P_1	k_7	$\frac{k_6}{k_5}$	k_4	k_4	k_3	k_3	$\frac{k_3}{k_2}$
P_2	k_7	$\frac{k_6}{k_5}$	k_4	k_4	k_3	$\frac{k_3}{k_2}$	k_1
P_3	$\frac{k_7}{k_6}$	k_5	k_4	k_3	k_2	k_1	k_1
P_4	$\frac{k_7}{k_6}$	$\frac{k_5}{k_4}$	k_3	k_2	k_1	k_1	k_1
P_5	$\frac{k_7}{k_6}$	$\frac{k_5}{k_4}$	$\frac{k_3}{k_2}$	k_1	k_1	k_1	k_1

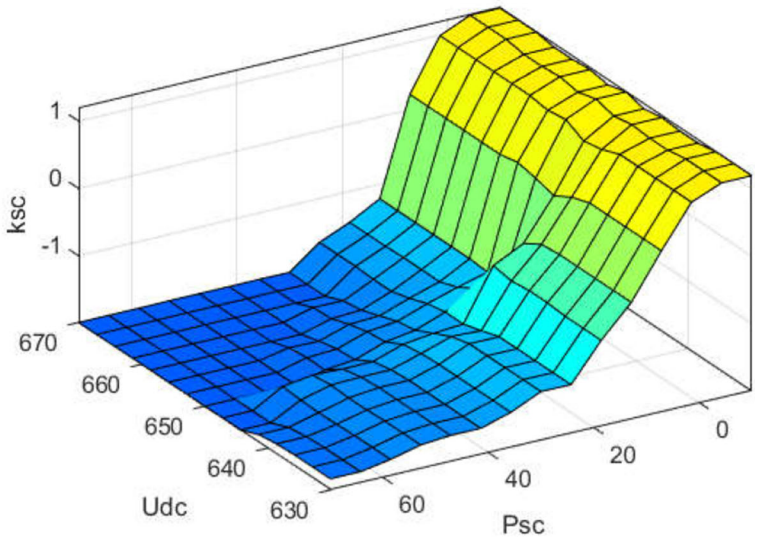

Figure 22. Surface observation graph of k_{sc}.

4. Variable Universe Fuzzy Control of HESSs Based on an Improved Harris Hawk Optimization Algorithm

4.1. Harris Hawk Optimization Algorithm

The Harris Hawk Optimization (HHO) Algorithm simulates the hunting strategy of real Harris Hawks in various scenarios through the creation of mathematical models [44]. The algorithm is structured into three main parts: the exploration phase, the exploitation phase, and the transition between the two phases.

4.1.1. Exploration Phase

During the exploration phase, Harris hawks utilize their keen eyesight to track and detect prey; however, locating prey can sometimes prove challenging. Consequently, the Harris hawk approaches potential prey by randomly selecting a position and calculating the vector difference between this prey position and the group's central position to determine the habitat location. Each individual Harris hawk serves as a candidate solution. In each iteration, the target prey represents the optimal solution to the problem, and the prey is identified using two strategies, as illustrated in Equation (19).

$$X(t+1) = \begin{cases} X_{\text{rand}}(t) - r_1|X_{\text{rand}}(t) - 2r_2X(t)|, q \geqslant 0.5 \\ (X_{\text{rabbit}}(t) - X_m(t)) - r_3(LB + r_4(UB - LB)), q < 0.5 \end{cases} \quad (19)$$

where t denotes the current iteration number, X(t + 1) denotes the position of the Harris Hawk at the t + 1 iteration; $X_{\text{rabbit}}(t)$ denotes the position of the prey at the t-th iteration; $X(t)$ denotes the position of the Harris Hawk at the t-th iteration; r_1, r_2, r_3, r_4, q are random numbers between 0 and 1; LB and UB denote the lower and upper bounds of the search space, respectively; $X_{\text{rand}}(t)$ denotes the position of the Harris Hawk selected randomly in

the population at the t-th iteration; $X_m(t)$ denotes the average value of the position of the Harris Hawk population at the t-th iteration, as shown in Equation (20):

$$X_m(t) = \frac{1}{N}\sum_{i=1}^{N} X_i(t) \tag{20}$$

where $X_i(t)$ denotes the position of the i-th Harris Hawk at the t-th iteration, N denotes the total number of Harris Hawks.

4.1.2. Transition Processes of Exploration and Exploitation Phase

As the prey continues to move, it transitions from an energetic state to a fatigued state. Inspired by this behavior, the HHO algorithm introduces a prey escape energy mechanism that facilitates the transition from the exploration stage to the exploitation stage. The HHO algorithm conceptualizes the prey's energy as escape energy, which decreases as the prey becomes more fatigued. Consequently, the escape energy can be expressed as shown in Equation (21), thereby enabling the algorithm to successfully transition from the exploration stage to the exploitation stage.

$$E = 2E_0\left(1 - \frac{t}{T}\right) \tag{21}$$

where E denotes the escape energy of the current prey; T denotes the maximum number of iterations; E_0 denotes the initial energy, which is a random number between (−1,1). During each iteration, when the escape energy $|E| \geq 1$, it enters the exploration phase; when the escape energy $|E| < 1$, it enters the exploitation phase.

4.1.3. Exploitation Phase

HHO proposed four strategies to simulate the attack of a Harris hawk. Using 'r' to represent the escape probability of prey.

Case 1: Soft Besiege

When $r \geq 0.5$ and $|E| \geq 0.5$, in this type of attack, the Harris's hawk flock will softly encircle it, making the prey more exhausted, and then make a surprise attack. The abstract mathematical model of this behavior is shown in Equations (22) and (23) as follows:

$$X(t+1) = \Delta X(t) - E \mid JX_{\text{rabbit}}(t) - X(t) \mid \tag{22}$$

$$\Delta X(t) = X_{\text{rabbit}}(t) - X(t) \tag{23}$$

The variable $\Delta X(t)$ represents the difference between the prey's position and the distance of the Harris hawk at the t-th iteration. J represents the random jump strength of the prey during the escape process, which is a random number between 0 and 2 that changes randomly in each iteration.

Case 2: Hard Besiege

When $r \geq 0.5$ and $|E| < 0.5$, the prey has low escape energy at this time, and the Harris Hawk directly carries out the final raid. In this case with Equation (24):

$$X(t+1) = X_{\text{rabbit}}(t) - E|\Delta X(t)| \tag{24}$$

Case 3: Soft Besiege with Progressive Rapid Dives

When $r < 0.5$ and $|E| \geq 0.5$, the prey still has enough energy to escape successfully. Before the raid, Harris Hawk established a soft siege strategy and integrated Levy flight into HHO. The position update strategy at this stage is shown in Equations (25)–(27):

$$Z = Y + S \cdot LF(D) \tag{25}$$

$$Y = X_{\text{rabbit}}(t) - E|JX_{\text{rabbit}}(t) - X(t)| \tag{26}$$

$$X(t+1) = \begin{cases} Y, F(Y) < F(X(t)) \\ Z, F(Z) < F(X(t)) \end{cases} \quad (27)$$

In the context of the current problem, let D represent the dimension, S represent a random row vector of D, Y represent the position vector calculated using the cumulative dive soft siege formula, Z represent the position disturbed by Levy flight, F(·) represent the function for finding the current fitness value, and LF(·) represent the disturbance value generated by Levy flight.

Case 4: Hard Besiege with Progressive Rapid Dives.

When r < 0.5 and |E| < 0.5, the prey does not have enough energy to escape, and the Harris Hawk will carry out a hard siege before the raid to capture the prey. During this siege, the Harris Hawk tried to reduce its distance from its prey, so updated as shown in Equations (28)–(30):

$$Z = Y + S \cdot LF(D) \quad (28)$$

$$Y = X_{\text{rabbit}}(t) - | EX_{\text{rabbit}}(t) - X_{\text{m}}(t) | \quad (29)$$

$$X(t+1) = \begin{cases} Y, F(Y) < F(X(t)) \\ Z, F(Z) < F(X(t)) \end{cases} \quad (30)$$

4.2. Proposed Algorithm and Its Numerical Experiments

The Fuch chaotic map is incorporated into the basic HHO algorithm for population initialization. To enhance both exploration and exploitation phases, the golden sine strategy and the lens imaging opposition-based learning strategy are introduced. The improved HHO algorithm, named MHHO, is evaluated on CEC2017 against other meta-heuristic algorithms like HHO, KOA, LSO, EO, and PKO to demonstrate its effectiveness.

4.2.1. Motivation for Algorithm Design

The HHO algorithm, while being an advanced optimization method with a straightforward structure, faces several challenges, including slow convergence speed, an inability to escape local optima, and low convergence accuracy. In meta-heuristic algorithms, the uneven distribution of the initial population can lead to issues such as diminished population quality and reduced diversity. To address this, the Fuch chaotic map is employed during the population initialization phase in place of traditional pseudo-random number generators, allowing for the generation of chaotic numbers between 0 and 1. This approach ensures that the initial solutions are more uniformly distributed across the solution space. When applying the HHO algorithm to optimize the scaling factor of variable universe fuzzy control, it is crucial to perform the optimization in an environment characterized by a small population and limited iterations. Therefore, to enhance the algorithm's optimization capabilities without increasing its computational time, it is essential to balance the exploration and exploitation phases. During the exploration phase, the golden sine strategy is incorporated to bolster the global exploration capabilities of the algorithm. In the exploitation phase, a novel elitism-based reverse learning strategy inspired by lens imaging principles is designed and integrated to prevent the algorithm from converging to local optima.

4.2.2. Fuch Mapping

The Tent map and Logistic map are two widely used chaotic maps in the field of chaos theory [53]. While Tent map exhibits good ergodicity, it has a minimum period and fixed point in its mathematical model, making it prone to local cycles and resulting in low chaotic efficiency. On the other hand, Logistic map has higher limitations and reaches its strongest chaotic state when the chaotic parameter is 4, but it lacks strong ergodicity. In contrast, Fuch chaotic map is a novel type of discrete chaotic map that showcases stronger chaotic characteristics and more balanced ergodicity [54]. In this study, we employ Fuch mapping as the mapping function for chaotic search, with its formula represented as Equation (31):

$$H_{n+1} = \cos(1/H_n^2) \tag{31}$$

where $H_n \in (-1,1)$ and $H_n \neq 0$, $n \in z^+$, $n = 1,2,\ldots,N$, n is the number of current iterations, and N is the maximum number of iterations. When $H_n = -0.6$, the Fuch map appears obvious chaotic phenomenon, and the mapping interval is $(-1, 1)$.

4.2.3. Golden Sine Strategy

The Golden Sine Algorithm (GSA) was introduced by Tanyildiz in 2017 [29]. This algorithm connects the sine function with the unit circle, enabling it to traverse all points on the circle. The process of scanning the complete unit circle is akin to searching in an optimization problem. Moreover, the introduction of the golden section coefficient in the update process allows each iteration to narrow the search range and explore the optimal solution region, thereby enhancing local mining ability and improving solution accuracy. The key aspect of the GSA algorithm lies in the method used to update the location of individuals. Initially, the location of n individuals is randomly generated, with each individual having an initial solution. The location of each individual is then updated using Equation (32):

$$X_i^{t+1} = X_i^t \cdot \left|\sin(r_1)\right| - r_2 \cdot \sin(r_1) \cdot \left|c_1 P_i^t - c_2 x_i^t\right| \tag{32}$$

where $X_i' = [X_{i,1}', X_{i,2}', \cdots, X_{i,d}']$, $(i = 1,2,\cdots,n; t = 1,2,\cdots,t_{\max})$, $X_{i,d}'$ represents the position of the i-th individual in the d-th dimension at the t-th iteration. P_i^t denote the coordinates of the global best individual at a specific iteration, while r_1 and r_2 are random numbers between 0 and 2π. The update equation incorporates parameters like c_1, c_2, $c_1 = a(1-g) + bg$, $c_2 = \mathrm{ag} + \mathrm{b}(1-\mathrm{g})$, a, and b, which are $[-\pi, \pi]$, g is the golden section number. The values of c_1 and c_2 help narrow down the search space and guide individuals towards the global optimal position during iteration. In the HHO algorithm, individuals that discover new species repeatedly achieve maximum fitness and guide the entire population. However, communication among discoverers is often lacking, a challenge that can be effectively addressed by the golden sine. The optimal state described in Equation (32) can lead other discoverers to this state, facilitating rapid transmission of crucial information. Equation (33) enables discoverers to explore neighboring regions for better solutions, ultimately reducing search range and accelerating algorithm convergence. Therefore, the Golden Synthetic strategy is beneficial for optimizing the discoverer's position. Following the introduction of Golden Synthetic, the population update mode of the HHO algorithm during the exploration phase is as follows:

$$\mathrm{X}(t+1) = \begin{cases} X_{rand} \cdot |\sin(r_1)| - r_2 \cdot \sin(r_1) |c_1 \mathrm{X}_{\mathrm{rand}}(t) - c_2 \mathrm{X}(t)|, q \geqslant 0.5 \\ (\mathrm{X}_{\mathrm{rabbit}}(t) - \mathrm{X}_m(t)) - r_3(LB + r_4(UB - LB)), q < 0.5 \end{cases} \tag{33}$$

4.2.4. Elitism Lens Imaging Opposition-Based Learning Strategy

In order to enhance the HHO algorithm's ability to escape local optima, a lens imaging opposition-based learning strategy is proposed based on the elitism principle. It operates on the assumption that for every feasible solution X in the solution space, there exists a corresponding opposition solution X^* If the fitness value of the opposition solution X^* surpasses that of the feasible solution X, the opposition solution X^* is then updated to the optimal solution.

Definition 1. *Opposition point [55]: Suppose that the position* $X_i = [X_i^1, X_i^2, \ldots, X_i^D]^{\mathrm{T}}$ *of the i-th solution is a point in D-dimensional space, and* $X_i^d = [a_d, b_d]$, $\mathrm{d} \in 1,2,\cdots\cdots,D$, *then the opposition point of* X_i *is denoted by* $X_i^* = [X_i^{1*}, X_i^{2*}, \ldots, X_i^{D^*}]^{\mathrm{T}}$, *where* $X_i^{d^*} = a_d + b_d - X_i^d$.

Definition 2. *Basis points [56]: If there are several points* $o_1, o_2, \cdots\cdots, o_M$ *in D-dimensional space, for any point* $X_i = [X_i^1, X_i^2, \ldots, X_i^D]^{\mathrm{T}}$, *the Euclidean distance from the reverse point* $X_i^* = [X_i^{1*}, X_i^{2*}, \ldots, X_i^{D^*}]^{\mathrm{T}}$ *to* $o_1, o_2, \cdots\cdots, o_M (m = 1, 2, \ldots, M)$ *is* l_M *and* l_M', *and we let the scaling factor* $k = l_m / l_m'$, *while k = 1, 2,. . ., n is called the basis point of X and H at k = m.*

The process of obtaining the opposition solution of the population in the solution space can be likened to the process of lens imaging, illustrated in Figure 23, showing the lens imaging opposition-based learning strategy. For instance, in a D-dimensional space scenario, suppose there is an object of height h located on X_i^d between $[a_d, b_d]$, and a convex lens with a focal length of r is positioned at the midpoint of the interval (referred to as basis point o_m). Through lens imaging, an image of height h′ is formed on the other side, with the coordinate projection point denoted as $X_i^{d^*}$. This imaging principle is shown:

$$\frac{\frac{(a_d+b_d)}{2} - X_i^d}{X_i^{d^*} - \frac{(a_d+b_d)}{2}} = \frac{h}{h'} \tag{34}$$

$$\frac{r}{X_i^{d^*} - \frac{(a_d+b_d)}{2} - r} = \frac{h}{h'} \tag{35}$$

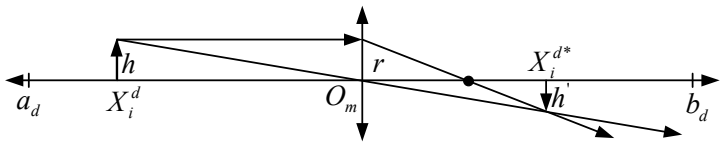

Figure 23. Lens imaging opposition-based learning strategy.

Using the similar triangle principle, the scaling factors $k = l_m/l'_m = h/h'$, Equations (36) and (37) are transformed into solving the inverse solution $X_i^{d^*}$, that is,

$$X_i^{d^*} = \frac{(a_d + b_d)}{2} + \frac{(a_d + b_d)}{2k} - \frac{X_i^d}{k} \tag{36}$$

$$X_i^{d^*} = (1 + 1/k)r + \frac{(a_d + b_d)}{2} \tag{37}$$

In Equation (37), when the position of the base point and the focal length r are held constant, a larger scaling factor k results in the reverse solution approaching the base point o_m and becoming closer to a feasible solution. This scaling factor, referred to as the micro-regulation factor, focuses on a narrow range around the feasible solution to enhance the diversity of the population. Following the principle of elitism, the newly generated solution and the global optimal solution are convexly combined with a ratio: α = 0.6.

$$X(t+1) = \alpha X_{best} + (1 - \alpha) X_i^{d^*} \tag{38}$$

The strategy is applied to Case 3 of HHO algorithm, known as cumulative dive soft siege, and Case 4, known as cumulative dive hard siege. After analyzing the new solution through the elitism lens imaging, the HHO algorithm's ability to escape local optima is enhanced by adjusting the scaling factor k, leading to accelerated convergence of the algorithm.

4.2.5. The Proposed MHHO Algorithm

The newly designed algorithm is named Golden Elite opposition-based learning Harris Hawk Optimization Algorithm, MHHO, the algorithm flow of MHHO is as follows:

Step 1: Set the algorithm initialization input parameters: the total number of population N, the maximum number of iterations Max_Iteration, convex combination factor α of 0.6;
Step 2: Using Fuch mapping (Equation (31)) to randomly generate the initial population;
Step 3: According to the fitness function, the initial population is evaluated;
Step 4: Calculate the fitness value: Calculate the fitness value of each particle individual, record and screen out the best population so far;
Step 5: Exploration and exploitation phase of the conversion strategy using Equation (21);
Step 6: Equation (33) is used in the exploration phase of the algorithm;
Step 7: Equations (22)–(38) are used in the exploitation phase of the algorithm;
Step 8: If the current number of iterations is less than the maximum number of iterations, the iteration process of step 5 and step 7 is repeated until the set accuracy requirement or

the maximum number of iterations is reached, and the optimal individual position and its fitness value are output.

4.2.6. Numerical Experiment

(1) Simulation environment

The simulation environment of this study runs on the Windows10 64-bit operating system. The CPU model is Intel(R) Xeon(R) CPU E5-2680 v3 @ 2.50 GHz and it is equipped with 64 GB RAM. The algorithm is implemented on the Matlab2020b platform.

(2) Benchmark functions and setting

To evaluate the efficacy of the MHHO proposed in this study, the CEC2017 benchmark function set was utilized. The CEC benchmark function comprises various basic test functions, serving not only as a benchmark for comparing optimization algorithms but also as a means to simulate real-world problem complexities [57]. The CEC2017 benchmark functions include 29 variations, encompassing unimodal functions like F1 and F3, multimodal functions from F4 to F10, mixed functions from F11 to F20, composite functions from F21 to F30, and excluding the high-dimensional unstable F2 function. The search range for the CEC2017 benchmark function set is [−100, 100] D. In the experiment, the algorithm's population size N is set to 50, the maximum number of iterations T is 500, the spatial search dimension Dim is 30, and the optimal fitness value for each experiment group is recorded.

(3) Comparative analysis of MHHO and other algorithms

CEC benchmark functions can effectively model the complexity of real-world problems, providing valuable insights for the development of new algorithms. To demonstrate the effectiveness of the algorithm proposed in this study, it is compared against three other meta-heuristic algorithms: MHHO, HHO, KOA [26], LSO [58], EO [28], and PKO [22]. The experiments are run independently 50 times, with the optimal fitness value recorded for each group. This value represents the function value of the test function, with the goal of the optimization algorithm being to minimize this value.

Table 3 presents the mean (**Mean**) and standard deviation (**Std**) of the optimal fitness for MHHO, HHO, KOA, LSO, EO, and PKO over 30 repetitions. The algorithm with the best mean and standard deviation for each test function is highlighted.

Table 3. Test results for CEC 2017.

Benchmarks		MHHO	HHO	KOA	LSO	×10O	PKO
F1	Mean	2.68×10^{7}	4.41×10^{8}	3.58×10^{10}	7.16×10^{10}	1.99×1010	6.67×10^{10}
	Std	7.86×10^{6}	2.47×10^{8}	7.74×10^{9}	1.13×10^{10}	4.83×10^{9}	7.99×10^{9}
	Rank	1	2	3	4	5	6
	Best	5.75×10^{7}	1.04×10^{9}	5.29×10^{10}	9.60×10^{10}	3.22×10^{10}	8.20×10^{10}
	Worst	1.39×10^{7}	6.99×10^{7}	2.06×10^{10}	5.10×10^{10}	8.05×10^{9}	5.48×10^{10}
F3	Mean	3.85×10^{4}	5.61×10^{4}	2.68×10^{5}	2.33×10^{5}	1.95×10^{5}	1.13×10^{5}
	Std	6.52×10^{3}	6.75×10^{3}	8.84×10^{4}	5.84×10^{4}	5.84×10^{4}	1.03×10^{4}
	Rank	1	2	4	6	3	5
	Best	5.37×10^{4}	6.80×10^{4}	5.45×10^{5}	3.53×10^{5}	3.88×10^{5}	1.26×10^{5}
	Worst	2.70×10^{4}	4.24×10^{4}	1.13×10^{5}	1.18×10^{5}	9.09×10^{4}	8.42×10^{4}
F4	Mean	5.45×10^{2}	7.40×10^{2}	7.97×10^{3}	2.27×10^{4}	3.66×10^{3}	1.79×10^{4}
	Std	2.96×10^{1}	1.33×10^{2}	2.74×10^{3}	5.50×10^{3}	1.49×10^{3}	3.95×10^{3}
	Rank	1	2	3	4	5	6
	Best	6.43×10^{2}	1.22×10^{3}	1.63×10^{4}	4.01×10^{4}	8.29×10^{3}	3.10×10^{4}
	Worst	4.83×10^{2}	5.58×10^{2}	3.04×10^{3}	1.16×10^{4}	1.71×10^{3}	1.15×10^{4}

Table 3. *Cont.*

Benchmarks		MHHO	HHO	KOA	LSO	×10O	PKO
F5	Mean	7.60×10^{2}	7.63×10^{2}	9.06×10^{2}	1.03×10^{3}	7.92×10^{2}	1.02×10^{3}
	Std	3.50×10^{1}	3.52×10^{1}	4.33×10^{1}	4.60×10^{1}	3.42×10^{1}	2.00×10^{1}
	Rank	1	2	3	4	5	6
	Best	8.26×10^{2}	8.34×10^{2}	9.97×10^{2}	1.14×10^{3}	8.74×10^{2}	1.06×10^{3}
	Worst	6.87×10^{2}	6.64×10^{2}	7.94×10^{2}	8.97×10^{2}	7.22×10^{2}	9.72×10^{2}
F6	Mean	6.67×10^{2}	6.67×10^{2}	6.85×10^{2}	7.13×10^{2}	6.55×10^{2}	7.14×10^{2}
	Std	5.79×10^{0}	5.79×10^{0}	1.06×10^{1}	8.82×10^{0}	7.92×10^{0}	4.64×10^{0}
	Rank	2	3	1	4	6	5
	Best	6.79×10^{2}	6.81×10^{2}	7.06×10^{2}	7.32×10^{2}	6.73×10^{2}	7.28×10^{2}
	Worst	6.46×10^{2}	6.56×10^{2}	6.59×10^{2}	6.92×10^{2}	6.36×10^{2}	6.99×10^{2}
F7	Mean	1.31×10^{3}	1.33×10^{3}	1.65×10^{3}	2.22×10^{3}	1.20×10^{3}	1.63×10^{3}
	Std	6.70×10^{1}	5.97×10^{1}	1.38×10^{2}	3.02×10^{2}	6.84×10^{1}	2.48×10^{1}
	Rank	2	3	1	5	4	6
	Best	1.42×10^{3}	1.43×10^{3}	1.93×10^{3}	2.72×10^{3}	1.31×10^{3}	1.66×10^{3}
	Worst	1.12×10^{3}	1.12×10^{3}	1.36×10^{3}	1.56×10^{3}	1.00×10^{3}	1.57×10^{3}
F8	Mean	9.72×10^{2}	9.92×10^{2}	1.17×10^{3}	1.28×10^{3}	1.07×10^{3}	1.22×10^{3}
	Std	2.40×10^{1}	2.63×10^{1}	3.68×10^{1}	3.77×10^{1}	2.71×10^{1}	3.05×10^{1}
	Rank	1	2	3	4	5	6
	Best	1.02×10^{3}	1.05×10^{3}	1.26×10^{3}	1.37×10^{3}	1.12×10^{3}	1.29×10^{3}
	Worst	9.28×10^{2}	9.23×10^{2}	1.07×10^{3}	1.20×10^{3}	9.97×10^{2}	1.17×10^{3}
F9	Mean	7.68×10^{3}	8.85×10^{3}	1.49×10^{4}	2.49×10^{4}	7.66×10^{3}	2.00×10^{4}
	Std	1.03×10^{3}	9.66×10^{2}	3.25×10^{3}	4.16×10^{3}	2.14×10^{3}	1.73×10^{3}
	Rank	2	3	1	4	5	6
	Best	1.02×10^{4}	1.12×10^{4}	2.41×10^{4}	3.48×10^{4}	1.36×10^{4}	2.44×10^{4}
	Worst	5.40×10^{3}	6.11×10^{3}	6.48×10^{3}	1.50×10^{4}	4.07×10^{3}	1.63×10^{4}
F10	Mean	5.80×10^{3}	6.18×10^{3}	9.70×10^{3}	9.89×10^{3}	9.30×10^{3}	8.92×10^{3}
	Std	5.98×10^{2}	7.34×10^{2}	4.07×10^{2}	4.13×10^{2}	6.33×10^{2}	3.30×10^{2}
	Rank	1	2	4	5	3	6
	Best	7.38×10^{3}	7.60×10^{3}	1.05×10^{4}	1.09×10^{4}	1.08×10^{4}	1.00×10^{4}
	Worst	4.57×10^{3}	4.67×10^{3}	8.63×10^{3}	8.84×10^{3}	7.76×10^{3}	8.36×10^{3}
F11	Mean	1.28×10^{3}	1.55×10^{3}	1.47×10^{4}	1.98×10^{4}	1.19×10^{4}	2.34×10^{4}
	Std	3.87×10^{1}	1.67×10^{2}	5.04×10^{3}	5.46×10^{3}	5.24×10^{3}	4.29×10^{3}
	Rank	1	2	3	4	6	5
	Best	1.36×10^{3}	2.23×10^{3}	2.80×10^{4}	3.22×10^{4}	3.11×10^{4}	3.83×10^{4}
	Worst	1.21×10^{3}	1.30×10^{3}	6.09×10^{3}	9.64×10^{3}	6.24×10^{3}	1.05×10^{4}
F12	Mean	2.45×10^{7}	7.06×10^{7}	4.97×10^{9}	1.31×10^{10}	1.65×10^{9}	2.00×10^{10}
	Std	1.89×10^{7}	4.92×10^{7}	1.50×10^{9}	3.72×10^{9}	7.31×10^{8}	1.69×10^{9}
	Rank	1	2	3	4	6	5
	Best	9.41×10^{7}	2.18×10^{8}	9.14×10^{9}	2.23×10^{10}	3.67×10^{9}	2.41×10^{10}
	Worst	2.91×10^{6}	8.36×10^{6}	2.52×10^{9}	5.22×10^{9}	2.92×10^{8}	1.60×10^{10}
F13	Mean	6.34×10^{5}	4.59×10^{6}	2.69×10^{9}	1.03×10^{10}	3.35×10^{8}	1.90×10^{10}
	Std	3.62×10^{5}	2.10×10^{7}	1.37×10^{9}	4.31×10^{9}	3.22×10^{8}	4.39×10^{9}
	Rank	1	2	3	4	6	5

Table 3. *Cont.*

Benchmarks		MHHO	HHO	KOA	LSO	×10O	PKO
F13	Best	1.85×10^{6}	1.49×10^{8}	6.77×10^{9}	1.91×10^{10}	1.29×10^{9}	3.36×10^{10}
	Worst	1.65×10^{5}	3.19×10^{5}	2.53×10^{8}	2.36×10^{9}	1.97×10^{7}	5.08×10^{9}
F14	Mean	5.72×10^{5}	1.15×10^{6}	6.72×10^{6}	1.22×10^{7}	2.37×10^{6}	1.30×10^{7}
	Std	6.53×10^{5}	1.28×10^{6}	4.65×10^{6}	9.04×10^{6}	2.69×10^{6}	3.64×10^{1}
	Rank	1	2	3	4	6	5
F15	Best	3.50×10^{6}	6.68×10^{6}	2.16×10^{7}	4.45×10^{7}	1.39×10^{7}	1.30×10^{7}
	Worst	1.39×10^{4}	1.72×10^{4}	4.38×10^{4}	1.29×10^{6}	8.29×10^{4}	1.30×10^{7}
	Mean	6.40×10^{4}	1.20×10^{5}	4.39×10^{8}	1.88×10^{9}	1.74×10^{7}	5.07×10^{9}
	Std	4.32×10^{4}	7.74×10^{4}	2.45×10^{8}	1.06×10^{9}	4.80×10^{7}	1.12×10^{9}
	Rank	1	2	3	4	6	5
F16	Best	2.25×10^{5}	4.98×10^{5}	1.16×10^{9}	5.04×10^{9}	3.37×10^{8}	6.52×10^{9}
	Worst	1.82×10^{4}	2.26×10^{4}	7.41×10^{7}	3.24×10^{8}	4.27×10^{5}	1.53×10^{9}
	Mean	3.62×10^{3}	3.73×10^{3}	4.88×10^{3}	6.14×10^{3}	3.83×10^{3}	6.26×10^{3}
	Std	4.32×10^{2}	5.31×10^{2}	4.01×10^{2}	5.79×10^{2}	3.40×10^{2}	5.44×10^{2}
	Rank	1	2	3	4	6	5
F17	Best	4.51×10^{3}	4.99×10^{3}	5.68×10^{3}	7.98×10^{3}	4.50×10^{3}	7.70×10^{3}
	Worst	2.62×10^{3}	2.63×10^{3}	3.80×10^{3}	5.16×10^{3}	3.11×10^{3}	5.32×10^{3}
	Mean	2.70×10^{3}	2.75×10^{3}	3.33×10^{3}	5.04×10^{3}	2.64×10^{3}	1.36×10^{4}
	Std	3.08×10^{2}	2.93×10^{2}	2.79×10^{2}	1.99×10^{3}	2.24×10^{2}	1.31×10^{4}
	Rank	2	3	1	4	6	5
F18	Best	3.59×10^{3}	3.36×10^{3}	4.02×10^{3}	1.31×10^{4}	3.10×10^{3}	5.92×10^{4}
	Worst	1.96×10^{3}	2.16×10^{3}	2.75×10^{3}	3.19×10^{3}	2.13×10^{3}	4.11×10^{3}
	Mean	1.51×10^{6}	4.54×10^{6}	7.06×10^{7}	1.33×10^{8}	1.75×10^{7}	1.18×10^{8}
	Std	1.40×10^{6}	6.71×10^{6}	4.72×10^{7}	8.25×10^{7}	2.02×10^{7}	8.05×10^{6}
	Rank	1	2	3	4	5	6
F19	Best	6.50×10^{6}	3.79×10^{7}	2.44×10^{8}	3.23×10^{8}	1.02×10^{8}	1.40×10^{8}
	Worst	1.09×10^{5}	1.44×10^{5}	6.26×10^{6}	1.92×10^{7}	1.14×10^{6}	7.10×10^{7}
	Mean	8.42×10^{5}	1.80×10^{6}	5.24×10^{8}	2.77×10^{9}	3.32×10^{7}	5.32×10^{9}
	Std	5.60×10^{5}	1.74×10^{6}	3.42×10^{8}	1.61×10^{9}	4.82×10^{7}	1.98×10^{9}
	Rank	1	2	3	4	6	5
F20	Best	2.62×10^{6}	1.05×10^{7}	1.53×10^{9}	6.40×10^{9}	2.91×10^{8}	6.65×10^{9}
	Worst	1.43×10^{5}	1.28×10^{5}	7.16×10^{7}	5.56×10^{8}	1.29×10^{6}	8.10×10^{8}
	Mean	2.84×10^{3}	2.76×10^{3}	3.37×10^{3}	3.44×10^{3}	3.05×10^{3}	3.44×10^{3}
	Std	2.32×10^{2}	2.36×10^{2}	1.60×10^{2}	1.83×10^{2}	2.23×10^{2}	6.45×10^{1}
	Rank	2	1	3	4	5	6
F21	Best	3.45×10^{3}	3.17×10^{3}	3.71×10^{3}	3.77×10^{3}	3.53×10^{3}	3.55×10^{3}
	Worst	2.31×10^{3}	2.27×10^{3}	2.95×10^{3}	3.08×10^{3}	2.61×10^{3}	3.18×10^{3}
	Mean	2.57×10^{3}	2.60×10^{3}	2.68×10^{3}	2.80×10^{3}	2.57×10^{3}	2.75×10^{3}
	Std	4.51×10^{1}	5.28×10^{1}	2.93×10^{1}	4.75×10^{1}	2.99×10^{1}	5.91×10^{1}
	Rank	2	3	1	4	5	6
F22	Best	2.68×10^{3}	2.71×10^{3}	2.76×10^{3}	2.91×10^{3}	2.64×10^{3}	2.84×10^{3}
	Worst	2.49×10^{3}	2.51×10^{3}	2.62×10^{3}	2.69×10^{3}	2.49×10^{3}	2.64×10^{3}
	Mean	7.52×10^{3}	6.98×10^{3}	1.04×10^{4}	1.11×10^{4}	8.98×10^{3}	9.48×10^{3}
	Std	7.32×10^{2}	1.60×10^{3}	1.23×10^{3}	6.78×10^{2}	2.66×10^{3}	6.34×10^{2}

Table 3. *Cont.*

Benchmarks		MHHO	HHO	KOA	LSO	×10O	PKO
F22	Rank	2	1	3	5	4	6
	Best	9.05×10^3	9.26×10^3	1.19×10^4	1.22×10^4	1.17×10^4	1.09×10^4
	Worst	4.50×10^3	2.56×10^3	6.35×10^3	8.26×10^3	3.86×10^3	8.28×10^3
F23	Mean	3.23×10^3	3.29×10^3	3.19×10^3	3.54×10^3	3.01×10^3	3.71×10^3
	Std	1.13×10^2	1.57×10^2	6.43×10^1	1.36×10^2	5.33×10^1	1.09×10^2
	Rank	3	4	1	2	6	5
	Best	3.51×10^3	3.67×10^3	3.35×10^3	3.92×10^3	3.13×10^3	3.90×10^3
	Worst	3.02×10^3	2.90×10^3	3.06×10^3	3.23×10^3	2.88×10^3	3.43×10^3
F24	Mean	3.65×10^3	3.49×10^3	3.35×10^3	3.75×10^3	3.17×10^3	4.07×10^3
	Std	1.90×10^2	1.72×10^2	7.63×10^1	1.34×10^2	4.71×10^1	1.84×10^2
	Rank	4	3	1	2	6	5
	Best	4.10×10^3	3.95×10^3	3.55×10^3	4.06×10^3	3.32×10^3	4.41×10^3
	Worst	3.22×10^3	3.14×10^3	3.20×10^3	3.49×10^3	3.08×10^3	3.62×10^3
F25	Mean	2.95×10^3	3.01×10^3	5.38×10^3	9.11×10^3	3.72×10^3	6.90×10^3
	Std	2.64×10^1	3.63×10^1	7.65×10^2	1.76×10^3	3.00×10^2	1.32×10^3
	Rank	1	2	3	4	5	6
	Best	3.03×10^3	3.09×10^3	7.64×10^3	1.41×10^4	4.62×10^3	9.17×10^3
	Worst	2.89×10^3	2.92×10^3	4.27×10^3	5.74×10^3	3.29×10^3	4.79×10^3
F26	Mean	7.93×10^3	8.28×10^3	9.23×10^3	1.22×10^4	7.54×10^3	1.21×10^4
	Std	1.15×10^3	1.09×10^3	8.13×10^2	1.16×10^3	5.73×10^2	6.13×10^2
	Rank	2	3	1	4	5	6
	Best	1.08×10^4	1.06×10^4	1.16×10^4	1.53×10^4	8.73×10^3	1.37×10^4
	Worst	3.08×10^3	3.30×10^3	7.75×10^3	9.45×10^3	5.82×10^3	1.07×10^4
F27	Mean	3.52×10^3	3.72×10^3	3.79×10^3	4.42×10^3	3.47×10^3	4.43×10^3
	Std	2.05×10^2	2.66×10^2	1.70×10^2	3.00×10^2	6.68×10^1	2.20×10^2
	Rank	2	3	1	4	6	5
	Best	4.20×10^3	4.89×10^3	4.25×10^3	5.21×10^3	3.64×10^3	4.85×10^3
	Worst	3.27×10^3	3.32×10^3	3.55×10^3	3.91×10^3	3.35×10^3	3.90×10^3
F28	Mean	3.31×10^3	3.48×10^3	6.36×10^3	8.91×10^3	4.80×10^3	7.35×10^3
	Std	2.20×10^1	9.20×10^1	8.07×10^2	1.11×10^3	5.02×10^2	7.27×10^2
	Rank	1	2	3	4	5	6
	Best	3.37×10^3	3.72×10^3	8.45×10^3	1.17×10^4	5.92×10^3	8.95×10^3
	Worst	3.26×10^3	3.36×10^3	4.89×10^3	6.26×10^3	4.01×10^3	6.17×10^3
F29	Mean	4.77×10^3	5.00×10^3	6.31×10^3	8.70×10^3	5.13×10^3	9.50×10^3
	Std	4.80×10^2	4.42×10^2	5.36×10^2	2.34×10^3	3.22×10^2	5.52×10^3
	Rank	1	2	3	4	6	5
	Best	5.87×10^3	6.08×10^3	7.60×10^3	2.03×10^4	5.87×10^3	4.54×10^4
	Worst	4.00×10^3	4.27×10^3	5.39×10^3	6.20×10^3	4.57×10^3	6.10×10^3
F30	Mean	3.81×10^6	1.40×10^7	3.38×10^8	1.53×10^9	5.77×10^7	4.82×10^9
	Std	2.46×10^6	1.84×10^7	1.62×10^8	6.06×10^8	5.07×10^7	1.83×10^9
	Rank	1	2	3	4	6	5
	Best	1.21×10^7	1.22×10^8	9.23×10^8	2.92×10^9	2.45×10^8	7.57×10^9
	Worst	4.46×10^5	1.90×10^6	9.68×10^7	3.85×10^8	4.53×10^6	8.53×10^8

The Wilcoxon rank sum test was used to evaluate the significance of MHHO compared to other algorithms at a 5% significance level, Its results are recorded in the Table 4. A result of $p < 5\%$ indicated a significant difference between the two algorithms, while a result above 5% was considered not significant. The rank sum test was applied to analyze the results, with symbols like '+', '−', and '=' indicating stronger, weaker, and similar optimization effects of MHHO in comparison to other algorithms. The results of the test in Friedman test are recorded in the AVR row at the bottom of the Table 4, and its ranking is recorded in the Rank row. The statistical results demonstrate that MHHO exhibits an absolute advantage over HHO, KOA, LSO, EO, and PKO. When comparing MHHO to HHO, it is found that the optimization performance is slightly inferior for no more than two benchmark functions. However, after implementing a multi-strategy joint improvement, MHHO showcases stronger convergence accuracy and stability compared to HHO, thereby validating the effectiveness of the enhanced strategy. From Figure 24, MHHO achieves the best mean and standard deviation when tested on unimodal functions, indicating its proficiency in handling such functions. For multi-peak functions F4 to F10, MHHO consistently outperforms other algorithms, except for F6, F7, and F9, showcasing its ability to avoid local optima. In the case of mixed functions F11 to F20 and composite functions F21 to F30, MHHO maintains a leading position in performance evaluation. While MHHO's performance on F20–F24 and F26–F27 in composite functions is slightly weaker, overall, the algorithm remains optimal when compared to other optimization algorithms, as confirmed by the Friedman test.

4.3. Variable Universe Fuzzy Control

Variable universe fuzzy control dynamically adjusts the size of the universe by introducing a scaling factor in fuzzy control. This allows the universe to shrink as the error decreases without altering the number of fuzzy rules. This approach aims to find the optimal balance between response speed and steady-state accuracy [59]. The modified domain can be represented as

$$X(x_i) = [-\alpha_i(x_i)\mathrm{E}_i, \alpha_i(x_i)\mathrm{E}_i] \tag{39}$$

$$Z(z_i) = [-\beta(z_i)\mathrm{U}, \beta(z_i)\mathrm{U}] \tag{40}$$

where $[-\mathrm{E}_i, \mathrm{E}_i]$ and $[-\mathrm{U}, \mathrm{U}]$ are the universes of discourse of input variables x_i and output variables z respectively; $\alpha_i(x_i)$ and $\beta(z_i)$ are the expansion factors of the domain X and Z respectively; compared with variable universe, E and U is the initial universe. As the universe shrinks, the peak distance of fuzzy division gradually decreases, thus enhancing the accuracy of the controller. The scaling factor for the input universe in fuzzy control is selected as

$$\alpha(x_i) = \varepsilon + \left(\frac{\|x_i\|}{E_i}\right)^{\tau_1}, \varepsilon > 0, \tau_1 > 0 \tag{41}$$

where x_i is the i-th input variable; ε is a very small constant.

The scaling factor of the output universe is selected as

$$\beta(z_i) = \varepsilon + \left(\frac{\|z_i\|}{U_i}\right)^{\tau_2}, \varepsilon > 0, \tau_2 > 0 \tag{42}$$

where z_i is the i-th output variable; ε is a very small constant.

Table 4. Results of Wilcoxon rank sum test and Friedman test.

Benchmarks	MHHO	HHO		KOA		LSO		EO		PKO	
		p-Value	+\=\−	*p*-Value	+\=\−	*p*-Value	+\=\−	*p*-Value	+\=\−	*p*-Value	+\=\−
F1	NA	7.56×10^{-10}	0\50\50	7.56×10^{-10}	0\50\50	7.56×10^{-10}	0\50\50	7.56×10^{-10}	0\50\50	7.56×10^{-10}	0\50\50
F3	NA	9.63×10^{-10}	2\50\48	7.56×10^{-10}	0\50\50	7.56×10^{-10}	0\50\50	7.56×10^{-10}	0\50\50	7.56×10^{-10}	0\50\50
F4	NA	8.03×10^{-10}	1\50\49	7.56×10^{-10}	0\50\50	7.56×10^{-10}	0\50\50	7.56×10^{-10}	0\50\50	7.56×10^{-10}	0\50\50
F5	NA	5.72×10^{-1}	24\50\26	7.56×10^{-10}	0\50\50	7.56×10^{-10}	0\50\50	1.64×10^{-4}	14\50\36	7.56×10^{-10}	0\50\50
F6	NA	6.89×10^{-1}	26\50\24	6.02×10^{-9}	6\50\44	7.56×10^{-10}	0\50\50	4.01×10^{-9}	47\50\3	7.56×10^{-10}	0\50\50
F7	NA	1.57×10^{-1}	19\50\31	7.56×10^{-10}	0\50\50	7.56×10^{-10}	0\50\50	1.42×10^{-8}	44\50\6	7.56×10^{-10}	0\50\50
F8	NA	2.49×10^{-4}	13\50\37	7.56×10^{-10}	0\50\50	7.56×10^{-10}	0\50\50	7.56×10^{-10}	0\50\50	7.56×10^{-10}	0\50\50
F9	NA	3.20×10^{-6}	10\50\40	8.03×10^{-10}	1\50\49	7.56×10^{-10}	0\50\50	3.57×10^{-1}	32\50\18	7.56×10^{-10}	0\50\50
F10	NA	1.79×10^{-3}	16\50\34	7.56×10^{-10}	0\50\50	7.56×10^{-10}	0\50\50	7.56×10^{-10}	0\50\50	7.56×10^{-10}	0\50\50
F11	NA	8.03×10^{-10}	1\50\49	7.56×10^{-10}	0\50\50	7.56×10^{-10}	0\50\50	7.56×10^{-10}	0\50\50	7.56×10^{-10}	0\50\50
F12	NA	1.29×10^{-6}	12\50\38	7.56×10^{-10}	0\50\50	7.56×10^{-10}	0\50\50	7.56×10^{-10}	0\50\50	7.56×10^{-10}	0\50\50
F13	NA	1.63×10^{-5}	9\50\41	7.56×10^{-10}	0\50\50	7.56×10^{-10}	0\50\50	7.56×10^{-10}	0\50\50	7.56×10^{-10}	0\50\50
F14	NA	2.18×10^{-3}	17\50\33	9.63×10^{-10}	2\50\48	1.02×10^{-9}	2\50\48	4.86×10^{-6}	11\50\39	7.56×10^{-10}	0\50\50
F15	NA	4.43×10^{-6}	10\50\40	7.56×10^{-10}	0\50\50	7.56×10^{-10}	0\50\50	7.56×10^{-10}	0\50\50	7.56×10^{-10}	0\50\50
F16	NA	2.90×10^{-1}	22\50\28	7.56×10^{-10}	0\50\50	7.56×10^{-10}	0\50\50	8.29×10^{-3}	19\50\31	7.56×10^{-10}	0\50\50
F17	NA	3.04×10^{-1}	24\50\26	1.66×10^{-9}	3\50\47	8.03×10^{-10}	1\50\49	2.57×10^{-1}	31\50\19	7.56×10^{-10}	0\50\50
F18	NA	3.89×10^{-4}	16\50\34	7.56×10^{-10}	0\50\50	7.56×10^{-10}	0\50\50	8.03×10^{-9}	6\50\44	7.56×10^{-10}	0\50\50
F19	NA	8.71×10^{-5}	13\50\37	7.56×10^{-10}	0\50\50	7.56×10^{-10}	0\50\50	7.56×10^{-10}	0\50\50	7.56×10^{-10}	0\50\50
F20	NA	1.72×10^{-1}	26\50\24	1.02×10^{-9}	2\50\48	1.30×10^{-9}	1\50\49	2.31×10^{-4}	14\50\36	8.03×10^{-10}	1\50\49
F21	NA	1.85×10^{-3}	14\50\36	7.56×10^{-10}	0\50\50	7.56×10^{-10}	0\50\50	8.43×10^{-1}	23\50\27	7.56×10^{-10}	0\50\50
F22	NA	9.40×10^{-2}	30\50\20	9.63×10^{-10}	2\50\48	7.56×10^{-10}	0\50\50	5.58×10^{-4}	14\50\36	7.56×10^{-10}	0\50\50
F23	NA	6.45×10^{-2}	18\50\32	3.02×10^{-2}	31\50\19	1.23×10^{-9}	2\50\48	8.03×10^{-10}	49\50\1	7.56×10^{-10}	0\50\50
F24	NA	1.02×10^{-4}	38\50\12	1.23×10^{-9}	49\50\1	2.64×10^{-3}	14\50\36	7.56×10^{-10}	50\50\0	3.17×10^{-9}	5\50\45
F25	NA	6.02×10^{-9}	4\50\46	7.56×10^{-10}	0\50\50	7.56×10^{-10}	0\50\50	7.56×10^{-10}	0\50\50	7.56×10^{-10}	0\50\50
F26	NA	1.17×10^{-1}	21\50\29	1.02×10^{-7}	5\50\45	7.56×10^{-10}	0\50\50	1.52×10^{-2}	32\50\18	7.56×10^{-10}	0\50\50
F27	NA	4.35×10^{-5}	11\50\39	1.40×10^{-7}	8\50\42	1.02×10^{-9}	1\50\49	2.37×10^{-1}	27\50\23	7.56×10^{-10}	0\50\50
F28	NA	7.56×10^{-10}	0\50\50	7.56×10^{-10}	0\50\50	7.56×10^{-10}	0\50\50	7.56×10^{-10}	0\50\50	7.56×10^{-10}	0\50\50
F29	NA	7.39×10^{-3}	16\50\34	7.56×10^{-10}	0\50\50	7.56×10^{-10}	0\50\50	6.05×10^{-5}	13\50\37	7.56×10^{-10}	0\50\50
F30	NA	1.50×10^{-8}	4\50\46	7.56×10^{-10}	0\50\50	7.56×10^{-10}	0\50\50	7.56×10^{-10}	0\50\50	7.56×10^{-10}	0\50\50
ARV	1.48	2.28		4.08		5.48		3.05		5.28	
Rank	1	2		4		6		3		5	

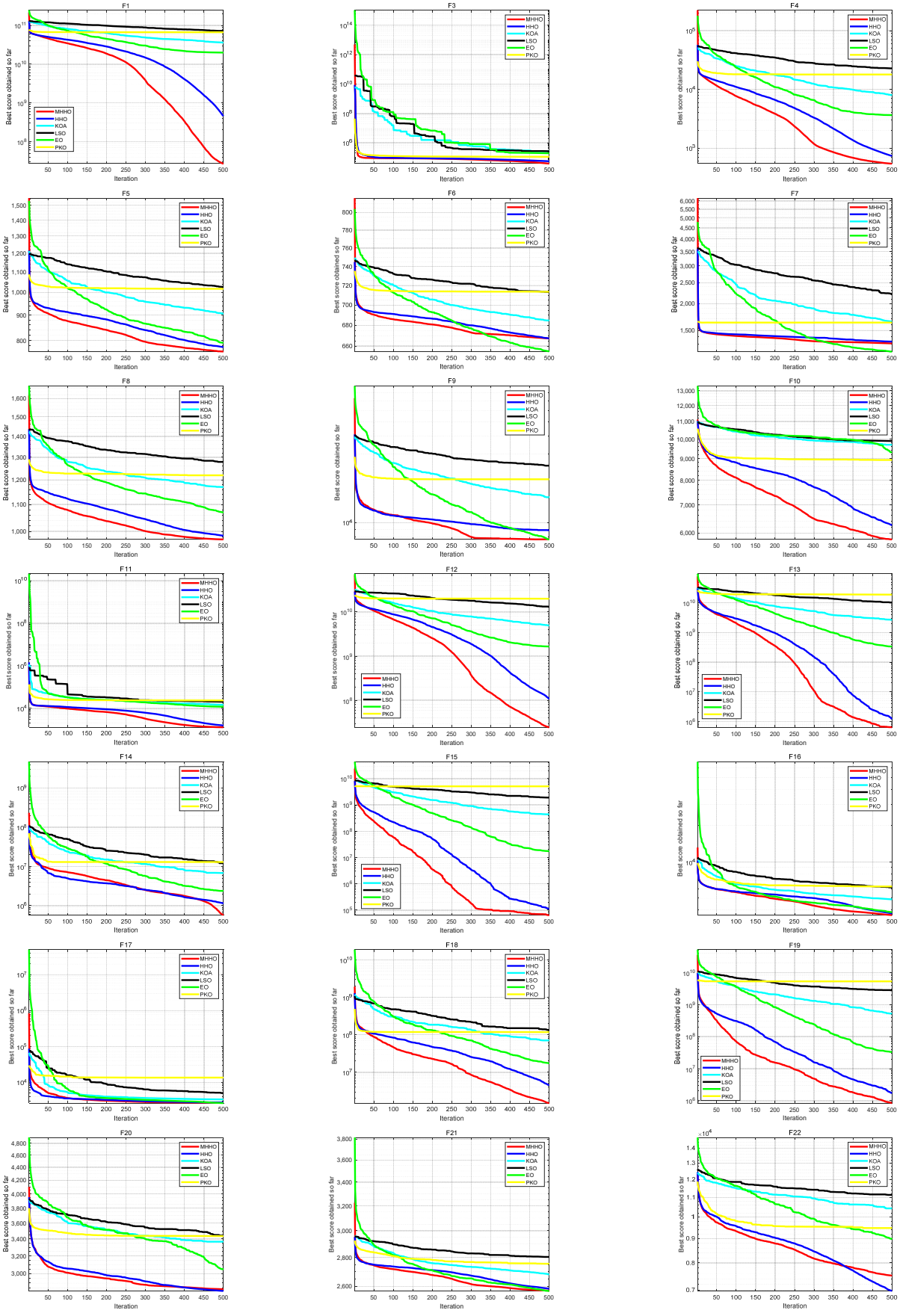

Figure 24. *Cont.*

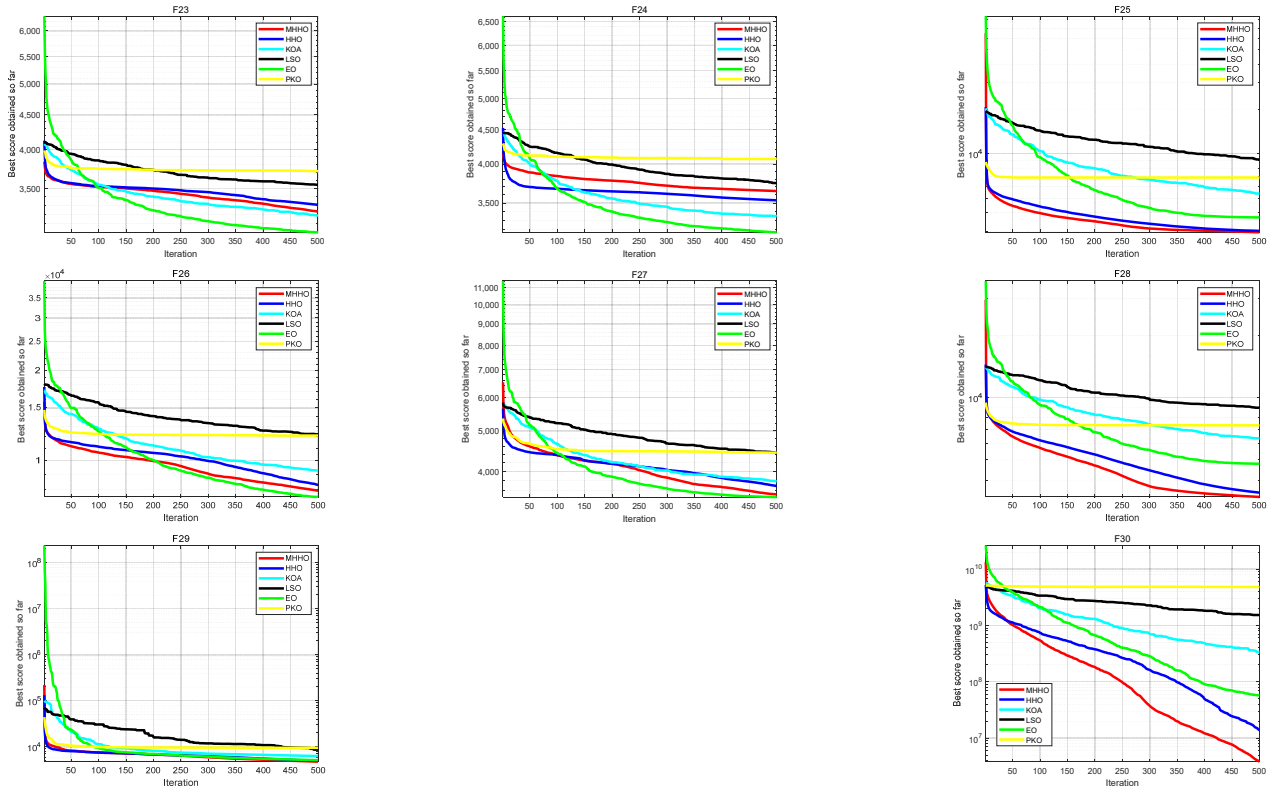

Figure 24. The convergence curves of the five algorithms on CEC2017.

4.4. Variable Universe Fuzzy Droop Control Based on an Improved HHO Algorithm

This paper employs the MHHO algorithm to self-tune the universe of fuzzy control based on the variable universe fuzzy control. The scaling factors of input and output variables are automatically adjusted according to the change in input deviation. This approach is applied to the fuzzy droop control system of HESSs in PV DC microgrid with HESSs, aiming to enhance the dynamic response capability and robustness of the system.

The input domain of the battery is defined as $X(u_{dc})$ and $X(P_{bat})$, and the input domain index parameters are τ_{u_dc} and τ_{P_bat} according to Equations (41)–(42). The domain of the output variable k_{bat} is $Z(k_{bat})$, and the output domain index parameter is τ_{bat}; similarly, the input domain of the super-capacitor is $X(u_{dc})$ and $X(P_{sc})$, according to the Equations (41)–(42), the input domain index parameter is τ_{u_dc} and τ_{P_sc}. The domain of the output variable k_{sc} is $Z(k_{sc})$, and the output domain index parameter is τ_{sc}. The MHHO algorithm is used to optimize the fuzzy control scaling factor (τ_{u_dc},τ_{P_bat},τ_{bat},τ_{u_dc},τ_{P_sc} and τ_{sc}) of the input and output universes in each sampling process. To assess the control effect, the voltage fluctuation is considered as the objective function in the variable universe fuzzy droop controller of the battery and super-capacitor. A smaller voltage fluctuation indicates better control characteristics.

4.5. Adaptive Variable Universe Fuzzy Droop Control Process Based on MHHO

The adaptive variable universe fuzzy droop control process of a PV DC microgrid with HESSs based on the MHHO algorithm is presented as fellow in accordance with the droop control requirements:

Step 1: Parameter initialization for MHHO algorithm;
Step 2: In the current control cycle, according to the output of the current controlled quantity, the voltage fluctuation of the bus, the P_{bat} of the battery branch and the P_{sc} of the super-capacitor branch are obtained;
Step 3: Taking the droop Equation (14) as the fitness function, the MHHO algorithm is used to optimize the scaling factor τ_{u_dc}, τ_{P_bat}, τ_{bat}, τ_{u_dc}, τ_{P_sc} and τ_{sc};

Step 4: Applying the optimal τ_{u_dc}, τ_{P_bat}, τ_{bat}, τ_{u_dc}, τ_{P_sc} and τ_{sc} which are obtained by the MHHO algorithm to the next control period of the droop control of the PV DC- microgrid with HESSs;
Step 5: If the control is over, stop; otherwise, go to Step 2.

5. Simulation and Results

In order to evaluate the effectiveness of the adaptive variable universe fuzzy-droop control strategy based on the MHHO algorithm, a simulation model of a PV DC microgrid (as depicted in Figure 25) is developed using the MATLAB 2022b/Simulink platform, CPU: Intel(R) Xeon(R) CPU E5-2680 v3 @ 2.50GHz, NVIDIA GeForce GTX 1060 3GB, Windows 10. Both energy storage converters in the system implement droop control. The DC bus voltage reference value is set at 650 V, with an allowable working range of 650 (±5%) V. Each converter operates at a switching frequency of 20 kHz, and the system parameters are detailed in Table 5.

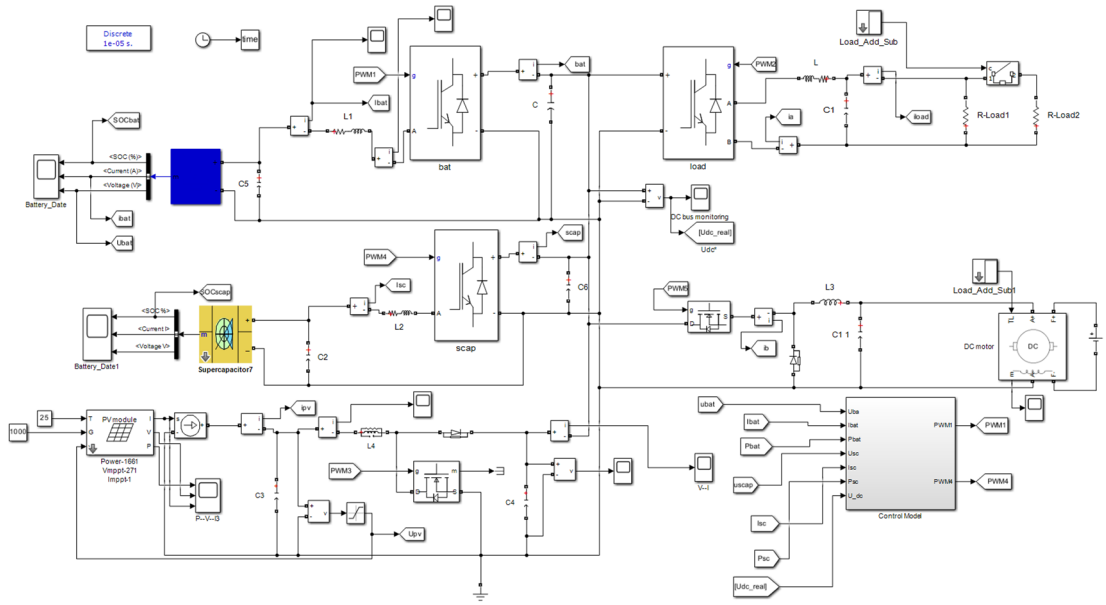

Figure 25. Simulation diagram of PV DC microgrid model.

Table 5. Parameters of PV DC microgrid.

Parameters	Value
DC bus capacitance/F	0.1
Battery rated voltage/V	200
Battery rated capacity/Ah	100
PV cell output voltage/V	400
SC rated capacity/F	20
SC rated voltage/V	380
DC bus voltage stability value/V	650
Initial droop coefficient of battery	0.2
Initial droop coefficient of super-capacitor	0.2

The PV cells in the DC microgrid simulation model output 7.5 kW, as depicted in Figure 26. Upon connection to the load at 0.4 s, the bus voltage experiences an instantaneous decrease, with the power change in the load portion illustrated in Figure 27. The steady-state power values are 5.6 kW under low load and 10.5 kW under high load, with a system power deficit of 3.0 kW. The energy storage unit charges during low load periods, while the deficit power of the system is compensated for by the battery and super-capacitor during high load scenarios.

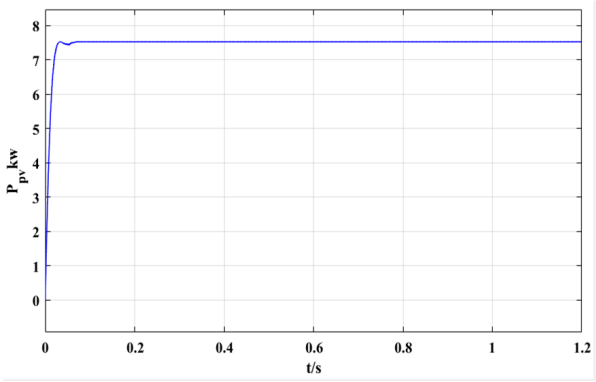

Figure 26. Output power of photovoltaic cell.

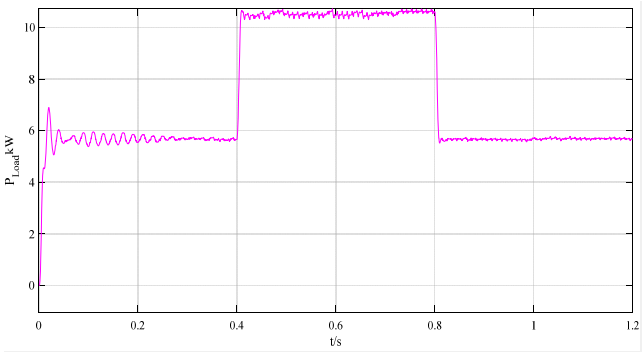

Figure 27. Power change curve of load part.

When the load is suddenly increased by 0.4 s, the energy storage unit is impacted by the droop control, leading to a quick power response. Figure 28 illustrates a comparison of power response curves for the battery branch under traditional droop control and fuzzy-droop control. Simulation results indicate that both control strategies result in power response oscillations, with peaks of approximately 4.0 kW and 3.5 kW at 0.45 s, respectively. Notably, the fuzzy-droop control minimizes power oscillation amplitudes, enhancing system disturbance rejection and response speed. Additionally, when the load is disconnected at 0.8 s, the battery power sharply drops to −0.17 kW under traditional droop control, causing significant vibration. In contrast, the adaptive fuzzy-droop control strategy shows faster system convergence post-disconnection. This strategy effectively enhances system dynamics, stability, and robustness in a PV DC microgrid. Power response curves for the SC branch under both control strategies are depicted in Figure 29. Figure 30 is the waveform of the DC bus voltage of the microgrid when the HESSs works in the adaptive variable universe fuzzy-droop control under the condition of load mutation.

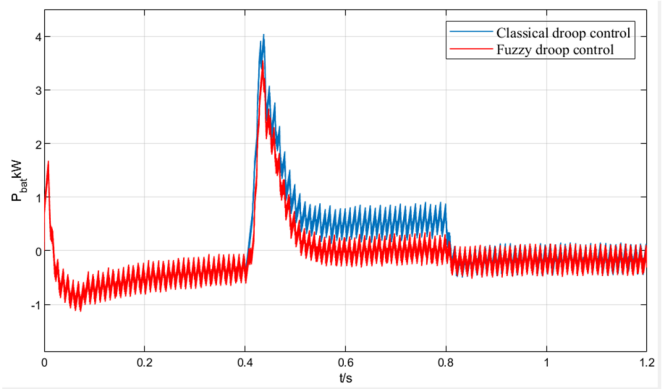

Figure 28. Comparison of power responses of battery branches.

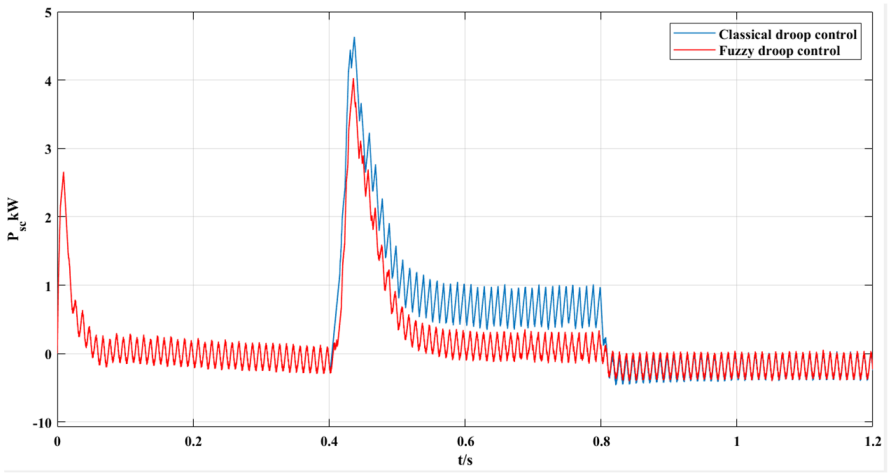

Figure 29. Comparison of power response curves of super-capacitor branches.

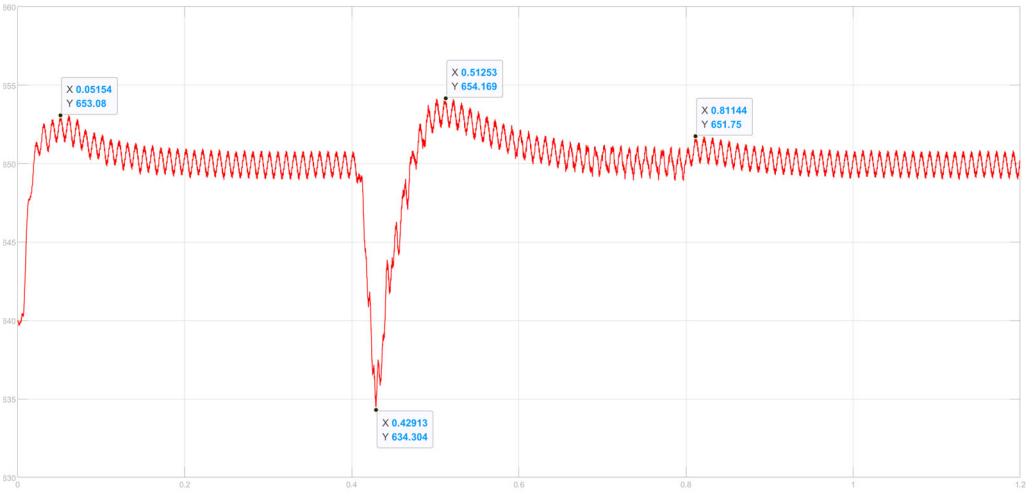

Figure 30. DC bus voltage of microgrid based on adaptive variable universe mode droop control.

When the load is connected at 0.4 s, the bus voltage instantaneously decreases. With droop control, the voltage drops by 18.30 V (see Figure 31). Using MHHO adaptive variable universe fuzzy droop control, the voltage drop is reduced to 15.70 V (see Figure 30). By compensating with the bus capacitor and HESSs, the bus voltage quickly rises above 650 V. The voltage increases by 4.4 V with droop control and by 4.1 V with MHHO adaptive variable universe fuzzy droop control. The bus voltage returns to 650 V around 0.65 s. Upon disconnecting the impulse load at 0.8 s, the droop control voltage rises by 4.2 V, the MHHO adaptive variable universe fuzzy droop control voltage rises by 1.75 V. The MHHO control shows a smaller increase compared to the traditional method. By utilizing bus capacitor absorption, the bus voltage returns to 650 V at 0.9 s. Simulation results demonstrate that the MHHO-based adaptive variable universe fuzzy droop control provides better voltage stabilization. Therefore, the adaptive fuzzy controller based on MHHO proves crucial in adjusting the droop coefficient.

In addition to the MHHO, the top two optimization algorithms, namely HHO and EO, have been selected from the six available optimization algorithms. These algorithms are applied to adaptive variable universe fuzzy-droop control, resulting in the development of adaptive HHO variable universe fuzzy droop control and adaptive EO variable universe fuzzy droop control. The result of adaptive HHO variable universe fuzzy droop control is illustrated in the Figure 32, The result of adaptive EO variable universe fuzzy droop control is illustrated in the Figure 33. The result indicate that the bus voltage experiences a drop of 17.0 V when the EO adaptive variable universe fuzzy droop control is employed,

representing 5% increase compared to the classical droop control method. In contrast, the results of HHO adaptive variable universe fuzzy droop control in a bus voltage drop of 16.1 V, which is 10% higher than the classical droop control method. Furthermore, the MHHO adaptive variable universe fuzzy droop control demonstrates a voltage drop that is 14.5% greater than that of the classical droop control method.

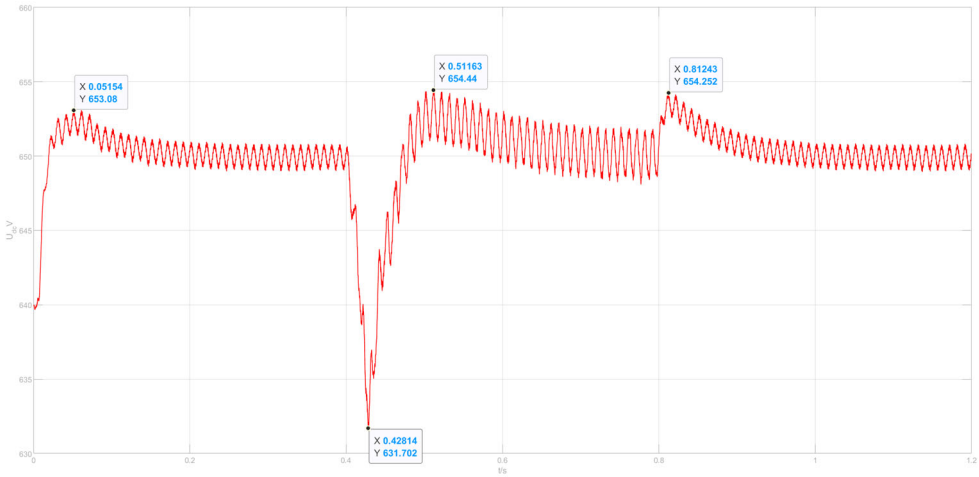

Figure 31. DC bus voltage of microgrid based on traditional droop control.

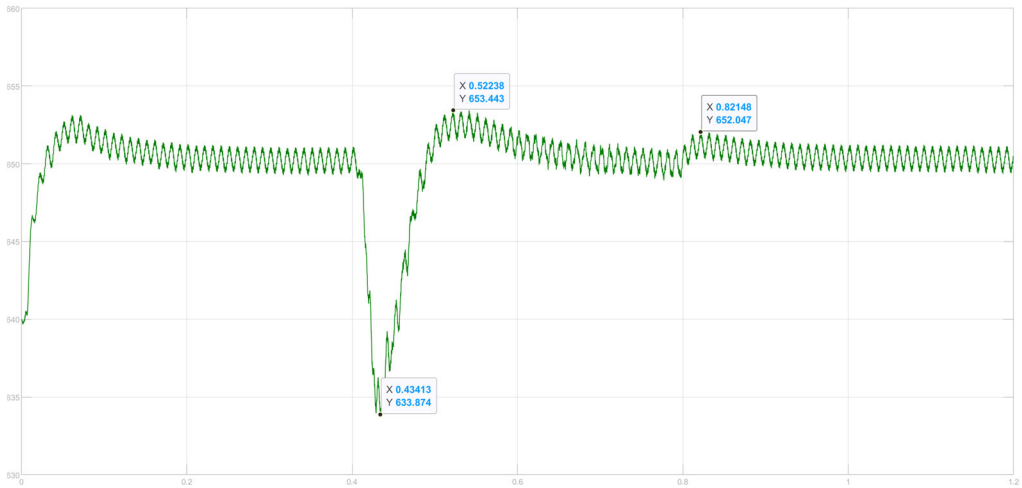

Figure 32. DC bus voltage of microgrid based on adaptive HHO variable universe mode droop control.

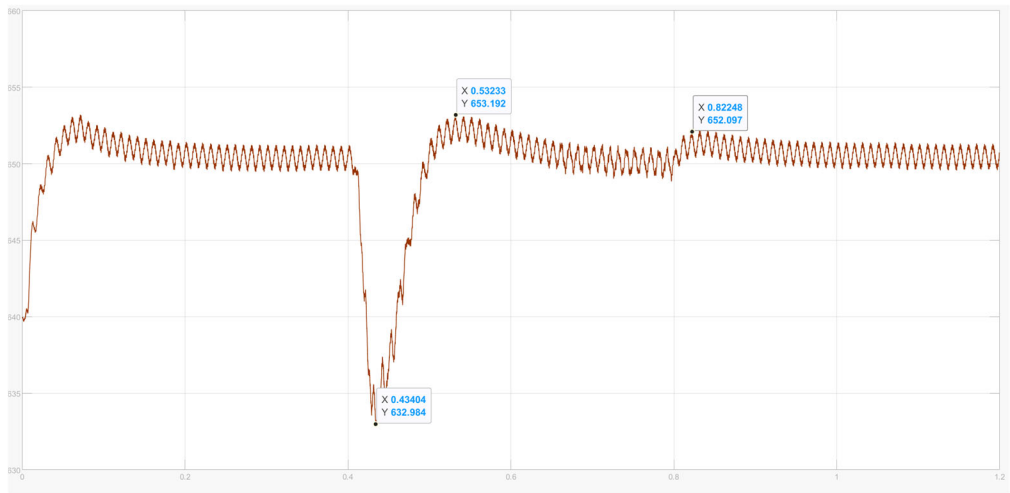

Figure 33. DC bus voltage of microgrid based on adaptive EO variable universe mode droop control.

In summary, the simulation results demonstrate that the hybrid energy storage system, utilizing adaptive MHHO fuzzy-droop control, effectively leverages the respective advantages of both batteries and SCs. In the event of sudden load changes, the fluctuation range of the bus voltage is constrained to $\pm 0.75\%$, thereby enhancing the system's dynamic response speed. Additionally, this approach facilitates the effective distribution of power fluctuations with varying frequency characteristics among the hybrid energy storage units. Overall, the adaptive fuzzy-droop control based MHHO not only mitigates bus voltage drops but also significantly enhances the system's capability to suppress bus voltage fluctuations.

6. Conclusions

The PV DC microgrid with HESSs has high reliability and can be deployed in remote areas to solve the problems of difficult power supply and low transmission and distribution efficiency. In the PV DC microgrid with HESSs, the study utilizes adaptive variable universe fuzzy control based on MHHO to enhance traditional droop control. This approach dynamically optimizes the droop coefficient in real-time, allowing the battery to effectively address low-frequency power shortages. Additionally, the super-capacitor is employed to manage high-frequency power shortages, mitigating the negative impact of internal factors like load fluctuations and line impedance on power distribution. By efficiently allocating power fluctuations with varying frequency characteristics among hybrid energy storage units, the system ensures safe and stable operation. The adaptive variable universe fuzzy control method based on MHHO is more stable and faster than the traditional droop method in ensuring bus voltage stability. The key findings are as follows:

1. The introduction of adaptive variable universe fuzzy control enhances the traditional droop control strategy, enabling dynamic adjustment of the initial droop curve coefficient for optimal power distribution.
2. The adaptive variable universe fuzzy-droop control based on MHHO outperforms traditional droop control by improving power distribution accuracy, reducing bus voltage fluctuations, and enhancing system robustness.
3. The MHHO algorithm demonstrates superior performance compared to HHO and other classical and new meta-heuristic algorithms with better performance like KOA, LSO, EO, and PKO.

Author Contributions: Conceptualization, C.W. and S.J.; methodology, C.W.; software, C.W.; validation, S.J., Y.Z. and X.W.; formal analysis, Y.L.; investigation, X.W.; resources, Y.Z.; data curation, S.J.; writing—original draft preparation, C.W.; writing—review and editing, S.J.; visualization, X.W.; supervision, Y.Z.; project administration, S.J.; funding acquisition, S.J. All authors have read and agreed to the published version of the manuscript.

Funding: This project was supported by the National Natural Science Foundation of China (Nos. 62371388, 62127809), Qin Chuangyuan Innovation Platform (No. 23TSPT0002), Scientists + Engineers Team (Nos. 23KGDW0011, 2024QCY-KXJ-014), and the Key Research Projects of Xi'an (No. 24LLRHZDZX0003).

Data Availability Statement: The original contributions presented in the study are included in the article, further inquiries can be directed to the corresponding author.

Conflicts of Interest: Author Xiaohui Wang was employed by the company Xi'an Thermal Power Research Institute Co., Ltd. The remaining authors declare that the research was conducted in the absence of any commercial or financial relationships that could be construed as a potential conflict of interest.

References

1. Papadimitriou, C.N.; Zountouridou, E.I.; Hatziargyriou, N.D. Review of Hierarchical Control in DC Microgrids. *Electr. Power Syst. Res.* **2015**, *122*, 159–167. [CrossRef]
2. Tian, G.; Zheng, Y.; Liu, G.; Zhang, J. SOC Balancing and Coordinated Control Based on Adaptive Droop Coefficient Algorithm for Energy Storage Units in DC Microgrid. *Energies* **2022**, *15*, 2943. [CrossRef]

3. Okwako, O.E.; Lin, Z.-H.; Xin, M.; Premkumar, K.; Rodgers, A.J. Neural Network Controlled Solar PV Battery Powered Unified Power Quality Conditioner for Grid Connected Operation. *Energies* **2022**, *15*, 6825. [CrossRef]
4. Lakhina, U.; Badruddin, N.; Elamvazuthi, I.; Jangra, A.; Huy, T.H.B.; Guerrero, J.M. An Enhanced Multi-Objective Optimizer for Stochastic Generation Optimization in Islanded Renewable Energy Microgrids. *Mathematics* **2023**, *11*, 2079. [CrossRef]
5. Chen, M.; Ma, S.; Wan, H.; Wu, J.; Jiang, Y. Distributed Control Strategy for DC Microgrids of Photovoltaic Energy Storage Systems in Off-Grid Operation. *Energies* **2018**, *11*, 2637. [CrossRef]
6. Tobajas, J.; Garcia-Torres, F.; Roncero-Sánchez, P.; Vázquez, J.; Bellatreche, L.; Nieto, E. Resilience-Oriented Schedule of Microgrids with Hybrid Energy Storage System Using Model Predictive Control. *Appl. Energy* **2022**, *306*, 118092. [CrossRef]
7. Lu, M.-Z.; Guo, Z.-W.; Liaw, C.-M. A Battery/Supercapacitor Hybrid Powered EV SRM Drive and Microgrid Incorporated Operations. *IEEE Trans. Transp. Electrif.* **2021**, *7*, 2848–2863. [CrossRef]
8. Yin, C.; Wu, H.; Locment, F.; Sechilariu, M. Energy Management of DC Microgrid Based on Photovoltaic Combined with Diesel Generator and Supercapacitor. *Energy Convers. Manag.* **2017**, *132*, 14–27. [CrossRef]
9. Dragicevic, T.; Guerrero, J.M.; Vasquez, J.C.; Skrlec, D. Supervisory Control of an Adaptive-Droop Regulated DC Microgrid with Battery Management Capability. *IEEE Trans. Power Electron.* **2014**, *29*, 695–706. [CrossRef]
10. Zhou, H.; Bhattacharya, T.; Tran, D.; Siew, T.S.T.; Khambadkone, A.M. Composite Energy Storage System Involving Battery and Ultracapacitor with Dynamic Energy Management in Microgrid Applications. *IEEE Trans. Power Electron.* **2011**, *26*, 923–930. [CrossRef]
11. Wang, S.; Tang, Y.; Shi, J.; Gong, K.; Liu, Y.; Ren, L.; Li, J. Design and Advanced Control Strategies of a Hybrid Energy Storage System for the Grid Integration of Wind Power Generations. *IET Renew. Power Gener.* **2015**, *9*, 89–98. [CrossRef]
12. Xiao, G.; Xu, F.; Tong, L.; Xu, H.; Zhu, P. A Hybrid Energy Storage System Based on Self-Adaptive Variational Mode Decomposition to Smooth Photovoltaic Power Fluctuation. *J. Energy Storage* **2022**, *55*, 105509. [CrossRef]
13. Anand, S.; Fernandes, B.G.; Guerrero, J. Distributed Control to Ensure Proportional Load Sharing and Improve Voltage Regulation in Low-Voltage DC Microgrids. *IEEE Trans. Power Electron.* **2013**, *28*, 1900–1913. [CrossRef]
14. Xiao, J.; Setyawan, L. Hierarchical Control of Hybrid Energy Storage System in DC Microgrids. *IEEE Trans. Ind. Electron.* **2015**, *62*, 4915–4924. [CrossRef]
15. Ding, M.; Lin, D.; Chen, Z.; Luo, Y.; Zhao, B. A Control Strategy for Hybrid Energy Storage Systems. *Proc. CSEE* **2012**, *32*, 1–6+184. [CrossRef]
16. Malik, S.M.; Sun, Y.; Hu, J. An Adaptive Virtual Capacitive Droop for Hybrid Energy Storage System in DC Microgrid. *J. Energy Storage* **2023**, *70*, 107809. [CrossRef]
17. Li, J.; Yang, Q.; Robinson, F.; Liang, F.; Zhang, M.; Yuan, W. Design and Test of a New Droop Control Algorithm for a SMES/Battery Hybrid Energy Storage System. *Energy* **2017**, *118*, 1110–1122. [CrossRef]
18. Vafamand, A.; Vafamand, N.; Zarei, J.; Razavi-Far, R.; Dragicevic, T. Intelligent Multiobjective NSBGA-II Control of Power Converters in DC Microgrids. *IEEE Trans. Ind. Electron.* **2021**, *68*, 10806–10814. [CrossRef]
19. Holland, J.H. Genetic Algorithms and the Optimal Allocation of Trials. *SIAM J. Comput.* **1973**, *2*, 88–105. [CrossRef]
20. Ahmad, M.F.; Isa, N.A.M.; Lim, W.H.; Ang, K.M. Differential Evolution: A Recent Review Based on State-of-the-Art Works. *Alex. Eng. J.* **2022**, *61*, 3831–3872. [CrossRef]
21. Kennedy, J.; Eberhart, R. Particle Swarm Optimization. In Proceedings of the ICNN'95—International Conference on Neural Networks, Perth, WA, Australia, 27 November–1 December 1995; IEEE: Piscataway, NJ, USA, 1995; Volume 4, pp. 1942–1948.
22. Bouaouda, A.; Hashim, F.A.; Sayouti, Y.; Hussien, A.G. Pied Kingfisher Optimizer: A New Bio-Inspired Algorithm for Solving Numerical Optimization and Industrial Engineering Problems. *Neural Comput. Appl.* **2024**, *16*, 1–59. [CrossRef]
23. Abdollahzadeh, B.; Gharehchopogh, F.S.; Khodadadi, N.; Mirjalili, S. Mountain Gazelle Optimizer: A New Nature-Inspired Metaheuristic Algorithm for Global Optimization Problems. *Adv. Eng. Softw.* **2022**, *174*, 103282. [CrossRef]
24. Harifi, S.; Mohammadzadeh, J.; Khalilian, M.; Ebrahimnejad, S. Giza Pyramids Construction: An Ancient-Inspired Metaheuristic Algorithm for Optimization. *Evol. Intell.* **2021**, *14*, 1743–1761. [CrossRef]
25. Ekinci, S.; Izci, D.; Yilmaz, M. Simulated Annealing Aided Artificial Hummingbird Optimizer for Infinite Impulse Response System Identification. *IEEE Access* **2023**, *11*, 88627–88636. [CrossRef]
26. Abdel-Basset, M.; Mohamed, R.; Azeem, S.A.A.; Jameel, M.; Abouhawwash, M. Kepler Optimization Algorithm: A New Metaheuristic Algorithm Inspired by Kepler's Laws of Planetary Motion. *Knowl.-Based Syst.* **2023**, *268*, 110454. [CrossRef]
27. Abdel-Basset, M.; Mohamed, R.; Sallam, K.M.; Chakrabortty, R.K. Light Spectrum Optimizer: A Novel Physics-Inspired Metaheuristic Optimization Algorithm. *Mathematics* **2022**, *10*, 3466. [CrossRef]
28. Faramarzi, A.; Heidarinejad, M.; Stephens, B.; Mirjalili, S. Equilibrium Optimizer: A Novel Optimization Algorithm. *Knowl.-Based Syst.* **2020**, *191*, 105190. [CrossRef]
29. Tanyildizi, E.; Demir, G. Golden Sine Algorithm: A Novel Math-Inspired Algorithm. *Adv. Electr. Comp. Eng.* **2017**, *17*, 71–78. [CrossRef]
30. Lam, A.Y.S.; Li, V.O.K. Chemical Reaction Optimization: A Tutorial: (Invited Paper). *Memetic Comput.* **2012**, *4*, 3–17. [CrossRef]
31. Talatahari, S.; Azizi, M.; Tolouei, M.; Talatahari, B.; Sareh, P. Crystal Structure Algorithm (CryStAl): A Metaheuristic Optimization Method. *IEEE Access* **2021**, *9*, 71244–71261. [CrossRef]
32. Trojovska, E.; Dehghani, M.; Trojovsky, P. Fennec Fox Optimization: A New Nature-Inspired Optimization Algorithm. *IEEE Access* **2022**, *10*, 84417–84443. [CrossRef]

33. Ray, T.; Liew, K.M. Society and Civilization: An Optimization Algorithm Based on the Simulation of Social Behavior. *IEEE Trans. Evol. Computat.* **2003**, *7*, 386–396. [CrossRef]
34. Sang, H.-Y.; Duan, P.-Y.; Li, J.-Q. An Effective Invasive Weed Optimization Algorithm for Scheduling Semiconductor Final Testing Problem. *Swarm Evol. Comput.* **2018**, *38*, 42–53. [CrossRef]
35. Liu, Y.; Liu, J.; Ma, L.; Tian, L. Artificial Root Foraging Optimizer Algorithm with Hybrid Strategies. *Saudi J. Biol. Sci.* **2017**, *24*, 268–275. [CrossRef]
36. Geem, Z.W.; Kim, J.H.; Loganathan, G.V. A New Heuristic Optimization Algorithm: Harmony Search. *Simulation* **2001**, *76*, 60–68. [CrossRef]
37. Mora-Gutiérrez, R.A.; Ramírez-Rodríguez, J.; Rincón-García, E.A. An Optimization Algorithm Inspired by Musical Composition. *Artif. Intell. Rev.* **2014**, *41*, 301–315. [CrossRef]
38. Moghdani, R.; Salimifard, K. Volleyball Premier League Algorithm. *Appl. Soft Comput.* **2018**, *64*, 161–185. [CrossRef]
39. Ma, B.; Hu, Y.; Lu, P.; Liu, Y. Running City Game Optimizer: A Game-Based Metaheuristic Optimization Algorithm for Global Optimization. *J. Comput. Des. Eng.* **2023**, *10*, 65–107. [CrossRef]
40. Abualigah, L.; Diabat, A.; Mirjalili, S.; Abd Elaziz, M.; Gandomi, A.H. The Arithmetic Optimization Algorithm. *Comput. Methods Appl. Mech. Eng.* **2021**, *376*, 113609. [CrossRef]
41. Mirjalili, S. SCA: A Sine Cosine Algorithm for Solving Optimization Problems. *Knowl.-Based Syst.* **2016**, *96*, 120–133. [CrossRef]
42. Pisinger, D.; Ropke, S. Large Neighborhood Search. In *Handbook of Metaheuristics*; Gendreau, M., Potvin, J.-Y., Eds.; International Series in Operations Research & Management Science; Springer: Boston, MA, USA, 2010; Volume 146, pp. 399–419. ISBN 978-1-4419-1663-1.
43. Yu, C.; Lahrichi, N.; Matta, A. Optimal Budget Allocation Policy for Tabu Search in Stochastic Simulation Optimization. *Comput. Oper. Res.* **2023**, *150*, 106046. [CrossRef]
44. Heidari, A.A.; Mirjalili, S.; Faris, H.; Aljarah, I.; Mafarja, M.; Chen, H. Harris Hawks Optimization: Algorithm and Applications. *Future Gener. Comput. Syst.* **2019**, *97*, 849–872. [CrossRef]
45. Luo, J.; Gao, S.; Wei, X.; Tian, Z. Adaptive Energy Management Strategy for High-Speed Railway Hybrid Energy Storage System Based on Double-Layer Fuzzy Logic Control. *Int. J. Electr. Power Energy Syst.* **2024**, *156*, 109739. [CrossRef]
46. Augustine, S.; Mishra, M.K.; Lakshminarasamma, N. A Unified Control Scheme for a Standalone Solar-PV Low Voltage DC Microgrid System With HESS. *IEEE J. Emerg. Sel. Top. Power Electron.* **2020**, *8*, 1351–1360. [CrossRef]
47. Celikel, R.; Yilmaz, M.; Gundogdu, A. A Voltage Scanning-Based MPPT Method for PV Power Systems under Complex Partial Shading Conditions. *Renew. Energy* **2022**, *184*, 361–373. [CrossRef]
48. Zhang, M.; Xu, Q.; Zhang, C.; Nordstrom, L.; Blaabjerg, F. Decentralized Coordination and Stabilization of Hybrid Energy Storage Systems in DC Microgrids. *IEEE Trans. Smart Grid* **2022**, *13*, 1751–1761. [CrossRef]
49. Ekinci, S.; Izci, D.; Yilmaz, M. Efficient Speed Control for DC Motors Using Novel Gazelle Simplex Optimizer. *IEEE Access* **2023**, *11*, 105830–105842. [CrossRef]
50. Cai, H.; Xiang, J.; Wei, W.; Chen, M.Z.Q. Droop Control for PV Sources in DC Microgrids. *IEEE Trans. Power Electron.* **2018**, *33*, 7708–7720. [CrossRef]
51. Xu, Q.; Hu, X.; Wang, P.; Xiao, J.; Tu, P.; Wen, C.; Lee, M.Y. A Decentralized Dynamic Power Sharing Strategy for Hybrid Energy Storage System in Autonomous DC Microgrid. *IEEE Trans. Ind. Electron.* **2017**, *64*, 5930–5941. [CrossRef]
52. Diaz, N.L.; Dragicevic, T.; Vasquez, J.C.; Guerrero, J.M. Intelligent Distributed Generation and Storage Units for DC Microgrids—A New Concept on Cooperative Control Without Communications Beyond Droop Control. *IEEE Trans. Smart Grid* **2014**, *5*, 2476–2485. [CrossRef]
53. Koupaei, J.A.; Hosseini, S.M.M.; Ghaini, F.M.M. A New Optimization Algorithm Based on Chaotic Maps and Golden Section Search Method. *Eng. Appl. Artif. Intell.* **2016**, *50*, 201–214. [CrossRef]
54. Li, L.; Liu, K.; Wang, L.; Sun, L.; Zhang, Z.; Guo, H. Fault Diagnosis of Balancing Machine Based on ISSA-ELM. *Comput. Intell. Neurosci.* **2022**, *2022*, 4981022. [CrossRef] [PubMed]
55. Tizhoosh, H.R. Opposition-Based Learning: A New Scheme for Machine Intelligence. In Proceedings of the International Conference on Computational Intelligence for Modelling, Control and Automation and International Conference on Intelligent Agents, Web Technologies and Internet Commerce (CIMCA-IAWTIC'06), Vienna, Austria, 28–30 November 2005; IEEE: Piscataway, NJ, USA, 2005; Volume 1, pp. 695–701.
56. Feng, W.; Zhang, W.; Huang, S. A Novel Parameter Estimation Method for PMSM by Using Chaotic Particle Swarm Optimization With Dynamic Self-Optimization. *IEEE Trans. Veh. Technol.* **2023**, *72*, 8424–8432. [CrossRef]
57. Abdel-Basset, M.; Mohamed, R.; Jameel, M.; Abouhawwash, M. Nutcracker Optimizer: A Novel Nature-Inspired Metaheuristic Algorithm for Global Optimization and Engineering Design Problems. *Knowl.-Based Syst.* **2023**, *262*, 110248. [CrossRef]
58. Shareef, H.; Ibrahim, A.A.; Mutlag, A.H. Lightning Search Algorithm. *Appl. Soft Comput.* **2015**, *36*, 315–333. [CrossRef]
59. Pang, H.; Liu, F.; Xu, Z. Variable Universe Fuzzy Control for Vehicle Semi-Active Suspension System with MR Damper Combining Fuzzy Neural Network and Particle Swarm Optimization. *Neurocomputing* **2018**, *306*, 130–140. [CrossRef]